

REVIEW

 View Article Online
View Journal | View Issue

 Cite this: *Mater. Chem. Front.*,
2024, 8, 903

Recent advances in metal-based electrocatalysts: from fundamentals and structural regulations to applications in anion-exchange membrane fuel cells

 Ali Han^a and Gang Liu^{id} *^{ab}

Alkaline exchange membrane fuel cells (AEMFCs) have broad application prospects due to the use of low-cost, non-precious catalysts. Furthermore, a wide range of fuels, for example, carbon-neutral hydrogen (H₂) and ammonia (NH₃), can be directly used in H₂-fueled AEMFCs and NH₃-fueled AEM direct ammonia fuel cells (AEM-DAFCs). However, the development of the above-mentioned AEMFCs is hindered by the sluggish dynamics of the alkaline hydrogen oxidation reaction (HOR), ammonium oxidation reaction (AOR), and oxygen reduction reaction (ORR) and low efficiency catalysts for these electrode reactions. Thus, it is expected that the rational design and controlled synthesis of highly efficient, durable catalysts will enable AEMFCs to achieve comparable performance to or even a higher performance than that of proton exchange membrane fuel cells (PEMFCs), which usually require high-cost platinum group metals (PGMs). In particular, the proposed catalytic mechanism of these reactions in alkaline media is still under debate, especially of the HOR and AOR. Herein, we present an in-depth, comprehensive understanding of the alkaline HOR, AOR, and ORR based on metal catalysts, especially employing PGM-free catalysts, including the proposed mechanisms and the current development of catalysts and AEMFCs. Finally, we highlight the prevailing challenge of the mechanisms and catalysts for each reaction and outline the possible development directions for AEMFCs. We anticipate that this review will offer global scientific insights and a roadmap for the design of catalysts for alkaline electrode reactions to accelerate the further development of AEMFC technology.

 Received 8th September 2023,
Accepted 10th November 2023

DOI: 10.1039/d3qm00947e

rsc.li/frontiers-materials

^a Shenyang National Laboratory for Materials Science, Institute of Metal Research, Chinese Academy of Sciences, 72 Wenhua Road, Shenyang, 110016, China.
E-mail: gangliu@imr.ac.cn

^b School of Materials Science and Engineering, University of Science and Technology of China, 72 Wenhua Road, Shenyang 110016, China

1. Introduction

Hydrogen (H₂) is a very promising, sustainable clean fuel as it only generates water when consumed in a fuel cell. However, to



Ali Han

Ali Han received her PhD from the School of Chemistry and Materials Science, University of Science and Technology of China (USTC) in 2016. She worked as a Postdoctoral Researcher at King Abdullah University of Science and Technology (KAUST) and Tsinghua University. Currently, she is a Professor of IMR, CAS. Her current research interests focus on the design of low-cost and effective electrocatalysts and devices for fuel cells.



Gang Liu

Gang Liu is a Professor and the Director of IMR, CAS. He received his Bachelor's Degree in Materials Physics from Jilin University in 2003 and PhD in Materials Science from IMR in 2009. His main research interest focuses on energy conversion materials and devices for fuels.



realize its commercial utilization, technical barriers pertaining to its transportation, storage, and distribution need to be urgently resolved. Thus, to address these complications and achieve a hydrogen economy, the utilization of hydrogen carriers has been proposed. Among the candidates for energy carriers, ammonia (NH_3) is promising because it is a popular commodity chemical and is stored, transported, and used worldwide.^{1,2} In contrast, the H_2 network is underdeveloped. Additionally, the NH_3 economy has also attracted attention due to the following advantages: (1) easy storage and transportation, (2) a high volumetric energy density, (3) low-cost H_2 carriers and a zero-carbon fuel; and (4) non-flammability. However, the main concern associated with NH_3 is its high toxicity compared to other types of energy sources; however, it can be detected by the human nose at concentrations as low as 1 ppm, allowing precautions to be taken in the event of a leak or spill. Hence, H_2/NH_3 -powered fuel cells are considered extremely promising energy conversion devices for mobile and stationary applications due to their great potential to be affordable, energy dense, and carbon neutral.

Generally, NH_3 can be directly utilized in direct ammonia fuel cells (DAFCs) or by supplying H_2 to H_2 -related fuel cells *via* thermal decomposition for low temperature alkaline exchange membrane fuel cells (AEMFCs).^{3,4} The major distinction between H_2 - and NH_3 -powered FCs is that H_2 can be used as anode fuels in an alkaline environment for AEMFCs and in acidic conditions for proton-exchange membrane fuel cells (PEMFCs), while NH_3 can only power AEM-DAFCs in alkaline media because only molecular NH_3 can be oxidized at the anode side besides the ammonium cation (NH_4^+). Fortunately, non-precious catalysts can be used at both the anode and cathode sides in less harsh alkaline operating conditions, which is superior to PEMFCs, where almost only platinum group metals (PGMs) can efficiently work on both electrode sides in harsh acid media. Moreover, PEMFCs require

perfluorinated membranes and high acid-tolerance stack hardware, resulting in extremely high cost. Thereby, AEMFCs are potentially low-cost alternatives to PEMFCs due to the use of less costly non-precious catalysts, alkaline membranes and stack hardware.

However, despite their great promise, AEMFCs are severely restrained by the lack of efficient electrocatalysts. In a typical H_2 -fueled AEMFC and NH_3 -fueled AEM-DAFC (Fig. 1), the same oxygen reduction reaction (ORR, $\text{O}_2 + 2\text{H}_2\text{O} + 4\text{e}^- = 4\text{OH}^-$) occurs on the cathode side of both cells. Also, the hydrogen oxidation reaction (HOR, $\text{H}_2 + 2\text{OH}^- = 2\text{H}_2\text{O} + 2\text{e}^-$) and ammonia oxidation reaction (AOR, $2\text{NH}_3 + 6\text{OH}^- = \text{N}_2 + 6\text{H}_2\text{O} + 6\text{e}^-$) occur on the former and latter cells, respectively. To date, PGM-free ORR catalysts have been intensively investigated, including transition metal oxides,^{5,6} metal-embedded nitrogen-doped carbon (M-N-C)⁷⁻¹⁰ and even metal-free catalysts,¹¹ which are anticipated to facilitate the fast development of AEMFC technology. However, there is a lack of efficient non-precious catalysts for the HOR and AOR. Hence, the prevailing challenge mainly comes from the anode side of alkaline HOR and AOR, in which PGMs still deliver the best HOR/AOR performance.¹²⁻¹⁸

Previous reports have demonstrated that the alkaline HOR activity is usually 2 orders of magnitude lower compared with that in the acid media, which requires higher loadings of PGMs to achieve the desired high performance for commercial applications and further increases the cost of AEMFCs.^{19,20} Thus, the HOR is the limiting reaction requiring more active PGM-free catalysts than Pt. Recently, Ni-based catalysts have been widely explored to exhibit the most active HOR performance among the PGM-free HOR alternatives.²¹⁻²⁵ However, Ni metal is easily oxidized under the operating conditions, leading to the generation of inescapable oxide species, which lower the activity. In this regard, research on the HOR mechanisms and activity descriptors in alkaline media can rationally guide the design for the development of high-efficient Ni-based HOR catalysts.

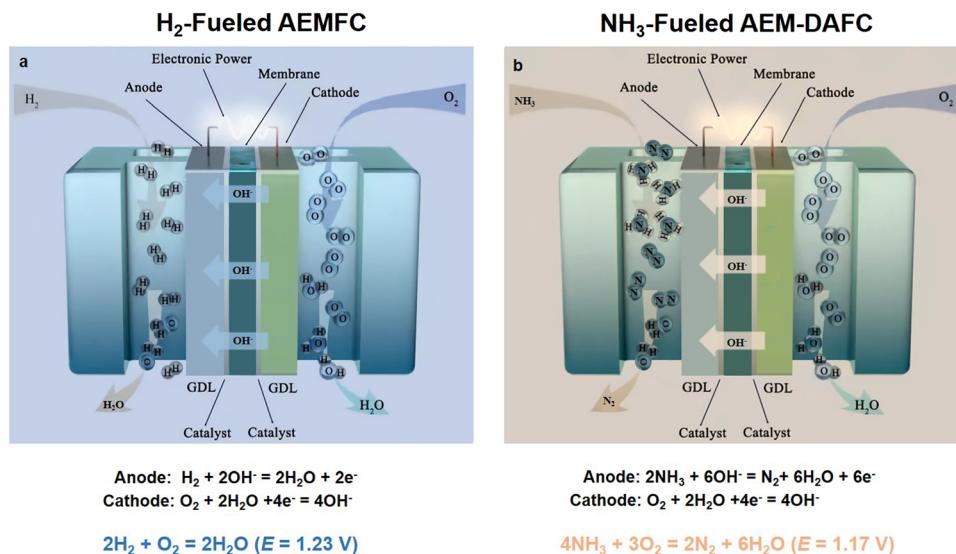


Fig. 1 A schematic view of the components and working principles of an H_2 -fueled AEMFC (a) and NH_3 -fueled AEM-DAFC (b).



- Alkaline membrane-based fuel cells (AMFCs).^{37,38}

Typically, NH₃-fueled-SOFCs require a high operating temperature to accelerate the decomposition of NH₃ at the anode side, which needs solid oxide electrolytes with PEM, AEM or molten hydroxides.^{32,39} When a PEM is used, the anode side reaction is: 2NH₃ → 3H₂ + N₂; H₂ → 2H⁺ + 2e⁻, while when an AEM is used, the anode side reaction is: 2NH₃ → 3H₂ + N₂; H₂ + O²⁻ → 2H₂O + 2e⁻. This type of system has shown great promise due to its high energy conversion efficiency, environmentally friendly nature, good fuel flexibility and good performance when H₂ is used as the fuel. However, for its practical application, several issues must be addressed, including the simultaneous formation of N₂ to dilute H₂ at the anode side and the corresponding formation of NO_x⁻ if N₂ reacts with oxygen species at high temperature.

The earliest type of AAFC was invented by Cairns *et al.* in 1968, using a KOH electrolyte to power the device at the operating temperature in the range of 50–200 °C.⁴⁰ Inspired by this work, extensive research has been conducted using molten hydroxide electrolytes for DAFCs.^{34,41,42} However, the durable performance of this type of fuel cell remains challenging because the strong reaction between CO₂ (from the air) and hydroxide electrolytes leads to the generation of carbonate ions such as K₂CO₃, which precipitate, lower the overall conductivity, and eventually poison the battery.

MAFCs are also alternative technology, which have gained attention due to their ability to process NH₃-contaminated wastewater, while simultaneously producing electricity. Generally, MAFC technology utilizes microorganisms to convert chemical energy from biodegradable materials into electricity.^{35,36} The DAFCs presented here are mainly the AEM-DAFC type, which utilize aqueous alkaline media according to a similar principle as AAFCs, give that they also operate by transferring OH⁻ ions and work at a relatively low temperature of 50–120 °C.^{37,38} Unlike NH₃-fueled-SOFCs, H₂ does not participate in the anode reaction. Instead, H₂O serves as an intermediate substance with the generated electric current, following eqn (2.4).

As shown in Fig. 1, in both fuel cells, O₂ molecules are reduced to OH⁻ at the cathode, and then reach the anode side *via* the AEM. In the case of the anode area in H₂-fueled AEMFCs, H₂ molecules are anodized and combined with OH⁻ to form H₂O, while NH₃ molecules are oxidized and combined with OH⁻ to form N₂ in NH₃-fueled DAFCs. Ultimately, an external circuit is formed by the electrons produced from the redox reactions on both sides of the electrode and powers the required devices. The thermodynamic voltage of NH₃-fueled DAFCs is 1.17 V (298 K). Similar to H₂-fueled AEMFC, the cell voltage of NH₃-fueled DAFCs often needs to overcome the slow electrode dynamics and the inevitable internal ohmic resistances.

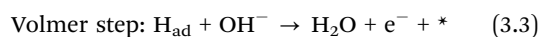
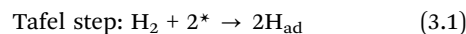
The device of AEM-DAFCs is assembled by coupling the anodic AOR *via* a 6e⁻ reaction process in alkaline aqueous solution:



3. Hydrogen oxidation reaction (HOR)

3.1. Mechanism understanding of HOR

HOR is the limiting reaction in H₂-fueled AEMFCs. In particular, Pt shows higher activity in HOR in acid media, whereas much slower activity in alkaline. Hence, it is a prerequisite to have deep insight into the HOR mechanism. Unlike HOR in acidic media, involving only protons, the alkaline HOR involves the formation of water. HOR in alkaline media follows three elementary steps, as follows:



where * represents the active site and H_{ad} refers to the adsorbed H atoms.

Four mechanisms are involved in HOR according to the rate-determining step (RDS). The kinetic expressions and Tafel slopes (TSs) are discussed in the following sections.

Volmer (RDS)–Tafel mechanism. In this mechanism, the Volmer step is the RDS and HOR exhibits the absolute TS value of 118 mV dec⁻¹, indicating a symmetric figure in the following Butler–Volmer (BV) fitting (3.4).

$$i = 2i_0 \left[\frac{-\alpha F}{e RT} \eta + \frac{\beta F}{e RT} \eta \right] (\alpha = \beta = 0.5) \quad (3.4)$$

where *i*₀ represents the exchange current.

Volmer–Tafel (RDS) mechanism. In the Volmer–Tafel (RDS) mechanism, the Tafel step is the RDS. However, the kinetics does not abide by the BV equation because the Tafel step does not involve charge transfer. Hence, HOR exhibits the absolute TS value of 30 mV dec⁻¹ according to the B–V fitting (3.5), as follows:

$$\eta = \frac{RT}{2F} \ln \left(1 + \frac{i}{i_T} \right) \quad (3.5)$$

Volmer (RDS)–Heyrovsky mechanism. In the Volmer (RDS)–Heyrovsky mechanism, the Volmer step is the RDS. HOR exhibits the absolute TS value of 39 mV dec⁻¹ according to the B–V fitting (3.6), as follows:

$$i = 2i_0 \left[\frac{-\alpha F}{e RT} \eta + e \frac{(1 + \beta)F}{RT} \eta \right] (\alpha = \beta = 0.5) \quad (3.6)$$

Volmer–Heyrovsky (RDS) mechanism. In the Volmer–Heyrovsky (RDS) mechanism, the Heyrovsky step is the RDS. HOR



exhibits the absolute TS value of 118 mV dec⁻¹ according to the B-V fitting (3.7), as follows.

$$i = 2i_0 \left[e^{-\frac{(1+\alpha)F}{RT}\eta} + e^{\frac{\beta F}{RT}\eta} \right] (\alpha = \beta = 0.5) \quad (3.7)$$

Notably, for the Volmer (RDS)-Tafel and Volmer-Heyrovsky (RDS) mechanisms, the Tafel slope has the same value (118 mV dec⁻¹), which makes it difficult to distinguish them. In addition, within the experimental uncertainty, the Tafel slope of the Volmer-Tafel (RDS) (30 mV dec⁻¹) and Volmer (RDS)-Heyrovsky (39 mV dec⁻¹) mechanisms is very close, which makes it difficult to draw conclusions of exclusivity to identify the specific reaction mechanism. Thereby, it is significant to employ other analytical methods to verify the HOR mechanism. The activity descriptor of HOR has been widely reviewed elsewhere,^{4,43-46} and hence it will not be highlighted here.

3.2. Recent electrocatalysts for HOR

PGM-related materials have been demonstrated to show efficient HOR performances in alkaline electrolyte, especially Pt and Ir.⁴⁷ However, the anode HOR activity of PGM catalysts is much slower in alkaline media than that in acid media (2-3 orders of magnitude).^{20,48} Thus, to obtain the desired AEMFC performance, the anode requires higher PGM loadings, offsetting the cost reduction of utilizing a PGM-free cathode. Hence, we mainly introduce the durable PGM-free HOR catalysts in this part to improve the eventual commercial development of H₂-fueled AEMFC technology. In the case of PGM-free HOR catalysts, only Ni-based catalysts have shown comparable HOR activity to Pt/C in alkaline media. Table 1 presents the HOR performance of PGM-free catalysts measured in alkaline electrolyte. Recently, increasing research advances have shown that in alkaline media, the typical HOR processes follow the Tafel-Volmer or Heyrovsky-Volmer mechanism.⁴⁹

3.2.1. Ni-N-related inorganic compounds. Yan *et al.* reported that nitrogen-doped carbon nanotube-supported Ni nanoparticles (NPs) showed HOR activity in alkaline media; however, their performance was still inferior to Pt catalysts.⁵⁰ Moreover, due to the relatively strong binding affinity of Ni to

oxygen, they suffered from low stability at potentials above 0.1 V vs. RHE, thereby seriously blocking their active sites. Thus, to obtain the required power output, HOR catalysts should work at potentials greater than 0.3 V relative to RHE.⁵¹ Recently, the investigated Ni-N-related catalysts are typically nickel nitrides or N-doped Ni-based catalysts, which have been intensively investigated to exhibit superior HOR activity compared to pure Ni species. The calculated results have demonstrated that introducing N heteroatoms can significantly enhance the HOR activity due to the optimal value of ΔG_{H} (~ 0) and decrease the activation energies of water formation and water dissociation. For example, Hu *et al.* reported the development of Ni₃N/C as an efficient HOR catalyst with superior HOR activity and stability compared to Ni.²² It was revealed that the Ni d band shifted down from Ni to Ni₃N and the interfacial charge shifted from Ni₃N to C, thereby weakening the hydrogen binding energy (HBE) and OH binding energy (OHBE), and enhancing the activity and stability of HOR. Recently, Wu *et al.* fabricated Mo-modified Ni₃N, which delivered much higher activity than pure Ni₃N for HOR.⁵² The MoO₂ and MoO₄²⁻ species were detected by *operando* Raman spectroscopy in the potential range of -0.2 V to 0.2 V vs. RHE. Also, these Mo-related species could significantly enhance the HOR catalytic performance by the weakened HBE and strengthened OHBE based on the bi-functional mechanism. Wang *et al.* reported that N-inserted Ni nanosheets exhibited enhanced HOR activity in alkaline media.⁵³ The mechanistic results demonstrated that N insertion in the Ni lattices could induce strong d-sp orbital hybridization, which could further facilitate the optimal adsorption of hydrogen intermediates. In addition, the surface strain derived from the lack of Ni-Ni coordination also enhanced the adsorption of OH species. The eventual modulation of the adsorption behaviors of the H and OH species significantly promoted the rate-determining Volmer step and triggered an excellent HOR performance. Later, they developed Ni-vacancy-rich Ni₃N (Ni₃N-r) as a platform for the arrangement of the Ni active center electrons in HOR.⁵⁴ Compared to the Ni₃N-vacancy-poor (Ni₃N-p) sample, the Ni ds-N 2p valence-electron-orbital interaction in the Ni₃N-r sample dramatically increased, thereby broadening the Ni ds valence-electron orbitals around the Ni vacancies in the Ni₃N-r

Table 1 A summary of the reported HOR catalytic performances of various PGM-free-related HOR catalysts measured in alkaline electrolytes

HOR catalysts	j_0 , ECSA ($\mu\text{A cm}^{-2}$)	j_k , Disk (mA cm^{-2})	$j_{\text{m}0}$ (A g^{-1})	$j_{\text{m}k}$ (A g^{-1})@50 mV	Ref.
Ni/V ₂ O ₃	38	—	—	42.1	<i>Angew. Chem., Int. Ed.</i> 2023, 62 , e202217275. ²¹
Ni ₃ N	80.08	11.09	—	—	<i>Nano Lett.</i> 2023, 23 , 107-115. ¹⁵⁹
Ni-H ₂ -NH ₃	70	4.55	—	59.2	<i>Nat. Mater.</i> 2022, 21 , 804-810. ²³
Ni _{5.2} WCu _{2.2}	14	—	2.54	2.55	<i>Nat. Commun.</i> 2021, 12 , 2686. ¹⁶⁰
Mo-Ni ₃ N	1.81	7.3	9.05	36.5	<i>ACS Appl. Nano Mater.</i> 2021, 4 , 11473-11479. ⁵²
Ni ₄ Mo	65	33.8	—	—	<i>Nat. Commun.</i> 2020, 11 , 4789. ⁶⁰
Ni-H ₂	2.9	5.85	24.41	50.4	<i>Angew. Chem., Int. Ed.</i> 2020, 59 , 10797-10801. ¹⁶¹
CeO ₂ (r)-Ni/C	38	1.73	—	12.3	<i>Angew. Chem., Int. Ed.</i> 2019, 58 , 14179-14183. ²⁵
Ni/NiO/C	26	1.59	—	5	<i>Angew. Chem., Int. Ed.</i> 2019, 58 , 10644-10649. ⁶³
Ni ₃ N/C	14	3.89	12.0	24.4	<i>Angew. Chem., Int. Ed.</i> 2019, 58 , 7445-7449. ²²
Ni/SC	40.2	1.52	7.4	11.0	<i>J. Mater. Chem. A</i> , 2019, 7 , 10936-10941. ¹⁶²
Ni/KB	28.6	—	7.0	—	<i>J. Electroanal. Chem.</i> 2019, 852 , 113551. ¹⁶³
Ni ₆ Cu ₄	34	—	—	—	<i>ACS Appl. Energy Mater.</i> 2019, 2 , 3160-3165. ¹⁶⁴



sample. Moreover, the integrated crystal orbital Hamiltonian population (COHP) of the Ni_{AC} ds-O 2p bonds in the Ni₃N-r sample showed an enhanced absolute value, indicating that the strengthened interactions could strengthen the OH binding at the Ni active centers. The weakened H binding and increased OH binding interactions in the Ni₃N-r sample were confirmed by the varying values of HBE and OHBE (Fig. 2a). The well-regulated H/OH binding interactions in the Ni₃N-r sample could notably lower the energy barrier (~ 0.73 eV), which was much lower than that of the Ni₃N-p (1.144 eV), as shown in Fig. 2b. This work shed new light on exploring HOR catalysts by regulating the electron arrangement of their active sites.

Recently, Hu and co-workers reported that an Ni-H₂-NH₃ HOR catalyst exhibited a record AEMFC performance. The Ni-H₂-NH₃ catalyst and reference catalysts were prepared by pyrolyzing the Ni-MOF at different mixture atmospheres, as shown in Fig. 2c. The choice of atmosphere showed a great influence on the size of the Ni NPs and their HOR performance.

As shown in Fig. 2d, the Ni-H₂-NH₃ catalyst exhibited the best HOR activity, which is even comparable with the commercial Pt/C. However, to date, whether OH⁻ is involved in HOR in alkaline media is still unclear. Thus, to demonstrate whether HBE and OHBE are involved in the present Ni-based catalysts, ultraviolet photoelectron spectroscopy (UPS) was further used to examine the Ni valence state in these three catalysts. The metallic nature of all the Ni samples was confirmed due to the passage of electron bands through the Fermi level (Fig. 2e). According to the *d*-band theory, the downward movement of the *d*-band leads to a weakened adsorption strength. Therefore, the HBE and OHBE of the catalysts followed the order of Ni > Ni-H₂ > Ni-H₂-NH₃ > Ni-NH₃. The HBE and OHBE experimental results were further demonstrated by H₂/OH chemisorption and isotope tests in 0.1 M KOD, matching well with the prediction of *d*-band theory. The correlation of the HOR activities with HBE and OHBE was obtained using the chemisorption binding constant as a proxy, as shown in Fig. 2f and g.

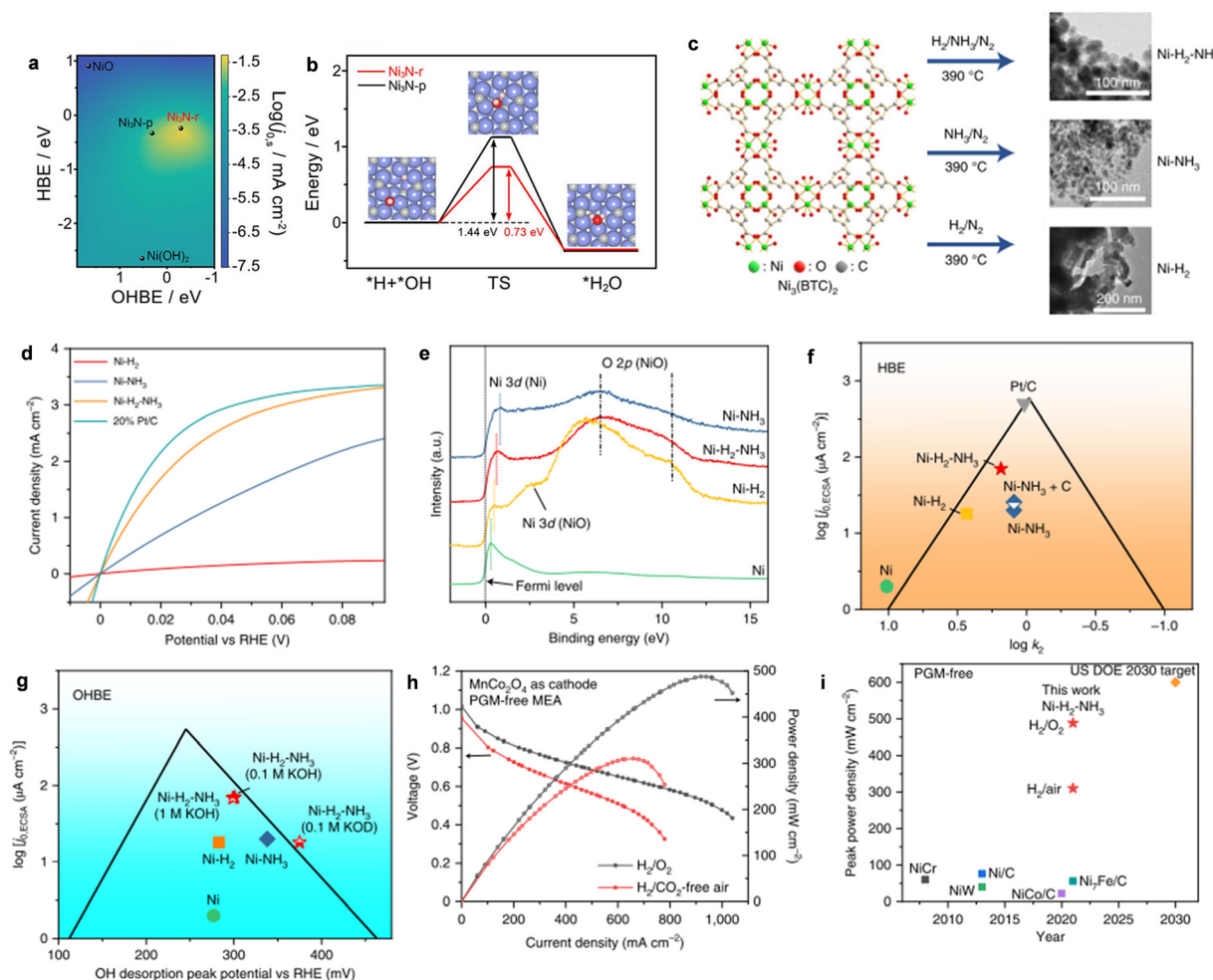


Fig. 2 (a) The logarithm of the HOR activity for different catalysts as a function of HBE and OHBE. (b) The combination of *OH and *H on Ni₃N-p and Ni₃N-r. Reproduced with permission from ref. 54 Copyright 2022, Wiley-VCH GmbH. (c) The synthesis of Ni-based catalysts. (d) HOR polarization curves for different catalysts. (e) UPS spectra analysis. The relationships of studied HOR activities with HBEs (f) and OHBEs (g). (h) The H₂-fueled AEMFC performance using Ni-H₂-NH₃ as the anode and CoMn spinel as the cathode. (i) A comparison of the PGM-free-based peak power density performance. Reproduced with permission from ref. 23 Copyright 2022, Nature Publications.



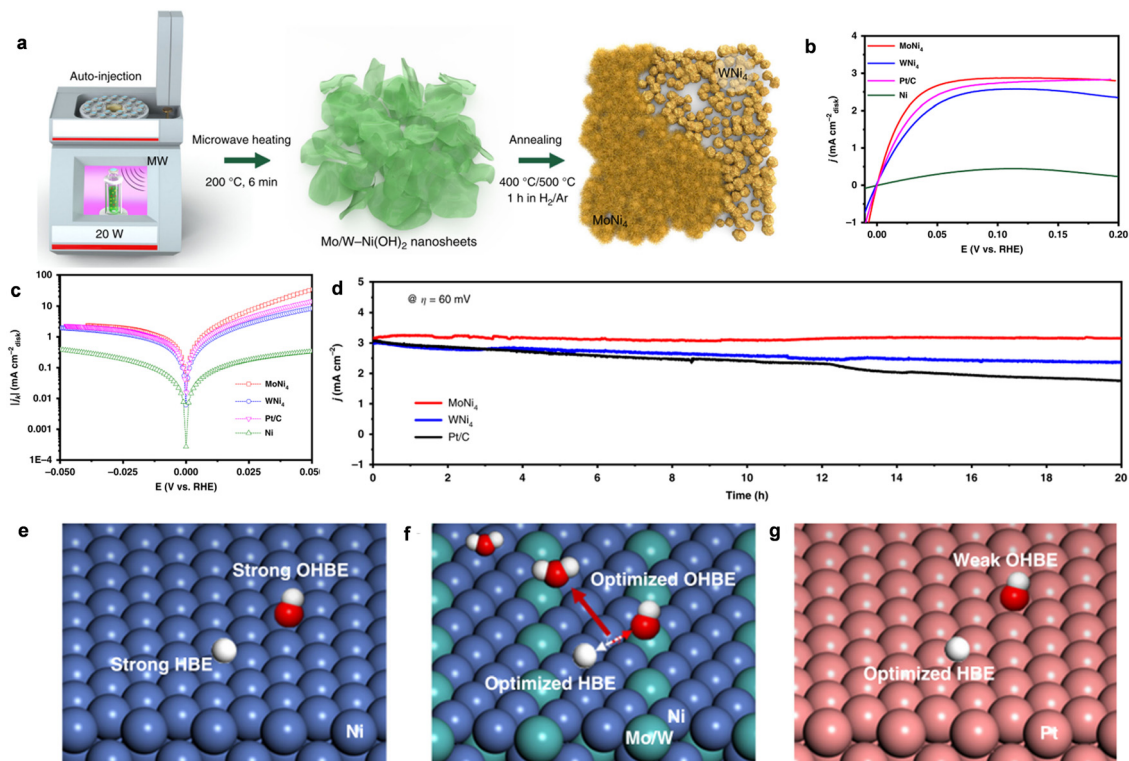


Fig. 3 (a) The synthesis of MoNi₄ and WNi₄ alloys. (b) The HOR polarization curves of different catalysts measured in H₂-saturated alkaline media. (c) The HOR/HER Tafel plots of the kinetic current density on MoNi₄, WNi₄, and reference catalysts in H₂-saturated alkaline media. (d) *i*-*t* responses recorded on MoNi₄, WNi₄, and Pt/C catalysts. (e)–(g) A schematic illustration of H and OH adsorption on different catalysts. Reproduced with permission from ref. 60 Copyright 2020, Nature Publications.

prepared *via* the reduction of Ni precursors in the presence of CeO₂ and XC-72. It was found that the amount of CeO₂ and oxygen vacancies in CeO₂ had a great influence on the enhanced HOR activity of Ni/C. The optimized HOR catalyst was labeled as CeO₂(-r)/Ni-1 in this work. The presence of oxygen vacancies in CeO₂ were confirmed by the of Raman spectra, as shown in Fig. 4a. The D band at 500–600 cm⁻¹ was attributed to the oxygen vacancies when partial Ce^{IV} changed into Ce^{III}, while the F_{2g} band at 458 cm⁻¹ represented the vibrational pattern of bulk CeO₂. The much higher intensity ratio value of the I_D/I_{F2g} bands for CeO₂(-r)/Ni-1 than that for CeO₂/Ni-1 indicated the presence of rich oxygen vacancies in CeO₂(-r)/Ni-1. The oxygen vacancies were also confirmed from the XPS spectra, as shown in Fig. 4b. The polarization curves in Fig. 4c show the superior performance of CeO₂(-r)/Ni-1 to CeO₂/Ni-1. The exchange current density of CeO₂(-r)/Ni-1 calculated using the BV equation is depicted in Fig. 4d and its *j*₀ value is much higher than that of CeO₂/Ni-1. These results demonstrated the critical role of oxygen vacancies in CeO₂ in determining the high activity of CeO₂(-r)/Ni-1 for HOR. The DFT results demonstrated that the adsorption free energies of H* (Δ*G*_{H*}) on pure Ni (111) was much higher than that on CeO₂(-r)/Ni (111), implying a much weaker HBE on Ni (111) after decoration with CeO₂(-r). The simulations also demonstrated the much stronger Δ*G*_{OH*} than pure Ni (111), indicating that the clear active interface could significantly promote the

adsorption of OH* on the surface of CeO₂(-r). The mechanism result is described in Fig. 4e, which showed that CeO₂(-r) could efficiently improve the OH* adsorption and optimize H*, well matching with the experimental enhanced HOR performance of CeO₂(-r)/Ni.

Recently, Yu and coworkers also fabricated high-activity HOR catalysts of Ni/V₂O₃ heterostructures.²¹ The Ni/V₂O₃ catalyst prepared by annealing the Ni-V hydroxide nanosheet arrays on nickel foam had abundant Ni and porous V₂O₃ interfaces after the thermal treatment process. The HOR polarization curves in Fig. 4f showed that Ni/V₂O₃ catalyst delivered the lowest onset potential (~0 V), accompanying the fastest increase in anodic current compared with pure Ni and V₂O₃, demonstrating the excellent activity for HOR in alkaline media. Importantly, the HOR performance was also comparable to commercial Pt/C catalyst. Besides, the Ni/V₂O₃ heterostructures also showed great durability and higher CO tolerance than Pt/C, indicating their potential for application for AEMFCs. The DFT calculations in Fig. 4g further demonstrated that the Ni/V₂O₃ heterostructures possessed the optimal HBE and OHBE, which could greatly promote the HOR activity in alkaline media. Particularly, compared with pure Ni HOR catalysts, the Ni oxidation around the Ni/V₂O₃ interface was dramatically suppressed after long-term stability test. The O adsorption energy was further obtained, as shown in Fig. 4h, indicating that the O species were inclined to adsorb on the pure Ni catalyst with a



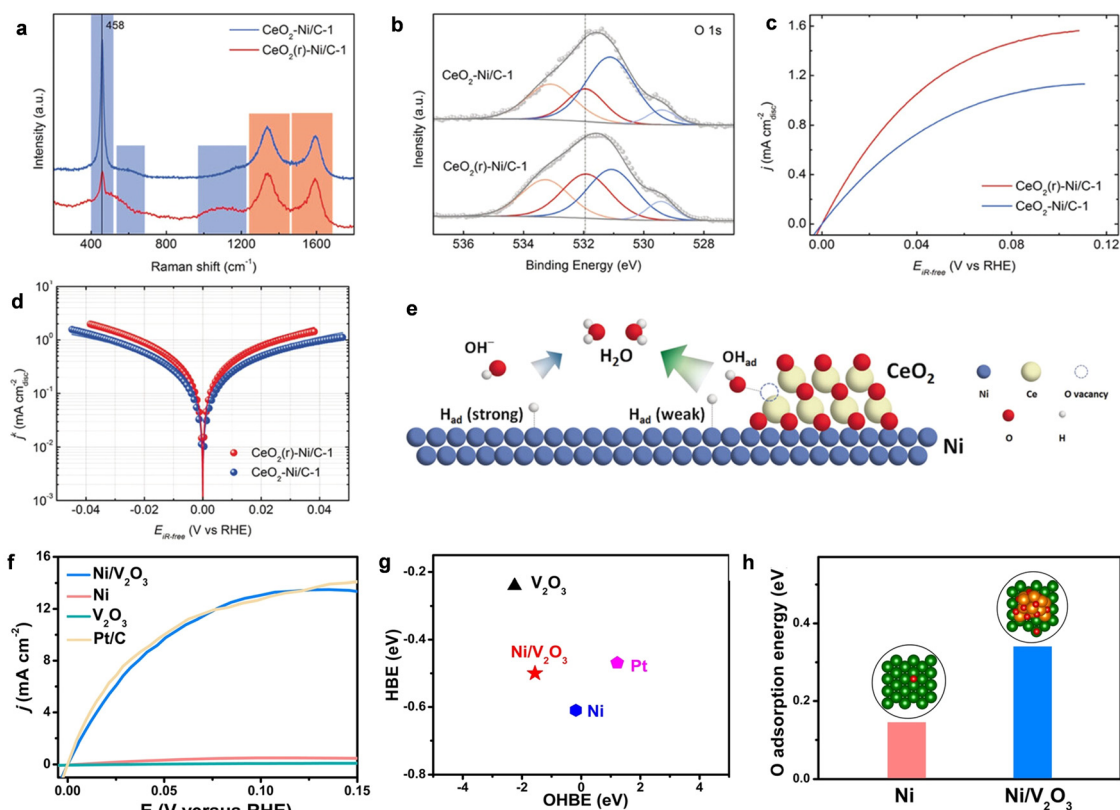


Fig. 4 (a) and (b) The Raman and XPS spectra of CeO_2 (r)-Ni/C-1 and CeO_2 -Ni/C-1, respectively. (c) HOR polarization curves for CeO_2 (r)-Ni/C-1 and CeO_2 -Ni/C-1. (d) The Tafel plots of CeO_2 (r)-Ni/C-1 and CeO_2 -Ni/C-1. (e) A schematic illustration of the role of O-vacancy-containing CeO_2 for the HOR. Reproduced with permission from ref. 25 Copyright 2019, Wiley-VCH GmbH. (f) The HOR polarization curves for different catalysts. (g) The simulated HBE and OHBE for different catalysts. (h) The simulated O adsorption energy of $\text{Ni}/\text{V}_2\text{O}_3$ and Ni. Reproduced with permission from ref. 21 Copyright 2023, Wiley-VCH GmbH.

low O adsorption energy of 0.15 eV, while the O adsorption energy on the $\text{Ni}/\text{V}_2\text{O}_3$ heterostructures was 0.34 eV. These results imply that the $\text{Ni}/\text{V}_2\text{O}_3$ heterostructure was much more difficult to be oxidized than pure Ni under the alkaline HOR condition.

4. Ammonia oxidation reaction (AOR)

Compared to water electrolysis, NH_3 decomposition ($\text{NH}_3 \rightarrow \text{N}_2 + \text{H}_2$) is a more efficient way to generate H_2 . For example, electrochemical water splitting requires a high voltage of 1.23 V to electrolyze the extremely stable H_2O molecules and convert them into the energy of 180 MJ to produce 1 kg H_2 . However, NH_3 decomposition only requires 33 MJ of energy to produce 1 kg H_2 . Thus, when NH_3 can be ideally attained in renewable ways (e.g., electrosynthesis and photosynthesis), NH_3 decomposition is expected to address the future energy shortage and make the utilization of H_2 more viable.

In previous studies, the focus of NH_3 has been on hydrogen production.^{69–71} However, the direct use of NH_3 as fuel is possible with the development of NH_3 -fuelled fuel cells (e.g., DAFCs). The direct integration of AOR in fuel cells not only alleviates the demand for on-board H_2 storage, but also effectively improves the whole processes.^{37,38,72} The simultaneous production of H_2 also favors the reduction of the electricity

demand by incorporating fuel cells. For example, Ezzat *et al.* proposed a route that used internal combustion engines to power vehicles fueled by NH_3 and H_2 (from NH_3 decomposition). The overall energy was found to be as high as 61.89%.⁷³ All these possible applications can further inspire studies in AOR beyond its use for H_2 generation.

4.1. Mechanism understanding for AOR

AOR mainly follows two recognized pathways, where the first is the O–S mechanism proposed by Oswin and Salomon.⁷⁴ Specifically, NH_3 is gradually dehydrogenated to $^*\text{N}$, and then N–N bonds bind to N_2 . The second is the G–M mechanism proposed by Gerischer and Mauerer.⁷⁵ In this case, NH_3 partial dehydrogenation generates dehydrogenation intermediates $^*\text{NH}_x$ ($x = 1, 2$), then dimerization generates hydrazine $^*\text{N}_2\text{H}_x$ ($x = 2, 3, 4$), and finally dehydrogenation produces N_2 . In both mechanisms, the reaction begins with the adsorption of ammonia and ends with the desorption of N_2 . In the intermediate steps, OH^- continuously oxidizes the dehydrogenation intermediates, while the formation of $^*\text{N}_2$ intermediates is the main cause of electrocatalyst poisoning. Compared with the O–S mechanism, the G–M mechanism is more widely accepted due to its lower onset potential, which has been demonstrated in many theoretical and experimental studies.^{76–79} For example, Gootzen *et al.* experimentally validated



the G–M mechanism for the first time to detect the reactive *NH_x intermediates and poisoning *N adsorbents by differential electrochemical mass spectrometry (DEMS).⁸⁰ Later, Vooy's *et al.* found that the adsorption strength of the metal to *N (M–N) follows the order of Ru > Rh > Pd > Ir > Pt > Au, Ag, Cu.⁸¹ Among the single metals, Pt showed the best activity for AOR, while Au, Ag, and Cu could not combine with *NH_x or *N . The N_2H_4 intermediate was further detected by Matsui *et al.* by *in situ* attenuated total reflection infrared spectroscopy (ATR-IR) under polarization.⁸² Additionally, Iglesias *et al.* recognized N_3^- by surface enhanced infrared spectroscopy (SERS) in the AOR process, which is a new reaction path involved in the G–M mechanism.⁷⁸ Additionally, Skachkov *et al.* found that two mechanisms can compete depending on the reaction potential.⁷⁶ The O–S mechanism was dominant at a moderate reaction potential (+0.5 V vs. RHE), while the G–M mechanism governed at a lower surface potential (<0.5 V vs. RHE).

Later, Herron *et al.* studied the catalytic AOR on different metals with close-packed surfaces by first-principles study.⁸³ They estimated the onset potentials of different metals, following the order of Co < Pd < Pt < Ir < Ni < Cu based on the G–M mechanism, as shown in Fig. 5a. Although Co showed the lowest onset potential, the simulated high N–N bond formation barriers severely limit the activity of Co for AOR. Based on the Sabatier analysis, the surface activity at 0 V against N–N binding formation barriers followed the order of Pt > Ir > Cu > Pd > Rh > Co, implying that Pt has the highest activity, followed by Ir (Fig. 5b). Based on the volcano plot found in this study, precious metals such as Pt, Pd and Ir are limited by their strong M–N bonds. In contrast, metals such as Au, Ag and Cu binds to N weakly; however, they are inactive for N_2 formation. Among the studied metals, Cu shows theoretically high AOR activity; however, a high overpotential of 1.22 V is required to lower the barrier of the electrochemical step due to the too weak Cu–N bond. Thus, it was concluded that Pt shows the best AOR activity followed by Ir and Cu and the optimal catalyst should process an M–N bond energy that is between Pt–N and Cu–N. Notably, the presence of the N–N coupling step and the strong *N adsorbent can result in the severe poisoning of the active surface. Besides the strong adsorbent of *N that can poison the

active surface, Matsui *et al.* found that the generation of oxygenated nitrides could also determine the whole AOR, as well as the tight interaction between *NO_x species and Pt surface could significantly hinder the formation of N_2 .⁸² Compared with direct H_2 /methanol fuel cells, DAFCs remain at a low technical level due to the more complicated and sluggish kinetic of AOR than the competing *H adsorption.² Consequently, in the design of catalysts for AOR with high efficiency, it is necessary to simultaneously suppress the H adsorption at the anode side of DAFCs.

4.2. Recent electrocatalysts for AOR

4.2.1. Molecular electrocatalysts.

Currently, there are three main types of electrocatalysts for AOR, including molecular catalysts, Pt-based precious metals and non-precious metal-related catalysts. The development of AOR by molecular electrocatalysts is rapid but still in its infancy.^{84–86} A recent review discussed the promising opportunities and gave new perspectives on the design of molecular catalysts with efficient activity for AOR.⁸⁷ Particularly, three critical parameters have been illustrated to design efficient molecular catalysts, namely, low N–H bond energy, favorable N_2 production dissociation and exergonic N–N coupling. In general, group IV–VI materials endowed with electron-rich characteristics show relatively low N–H bond energies, probably due to their strong ability to produce multiple metal–ligand bonds and tendency to form high oxidation states. Unlike the previously known Ru-based noble molecular electrocatalysts, Zott *et al.* reported the preparation of first-row iron(II) tris(2-pyridylmethyl)amine (TPA) bis-ammine triflate AOR electrocatalysts,⁸⁴ as shown in Fig. 6a. Cyclic voltammetry experiments indicated that in the presence of NH_3 , the onset potential was obvious under the condition of 0.7 V vs. Fc/Fc^+ , and the attenuation of catalytic current was negligible after 50 continuous cyclic voltammetry (CV) cycles, indicating the robust stability of TPA-connected Fe to AOR (Fig. 6b). In contrast, there was a continuous decrease in the peak current using $FeOTf_2$ as the anode catalyst, which was attributed to the instability of $[Fe(NH_3)_6]OTf_2$ (formed by $FeOTf_2$ existing in the presence of NH_3) under the catalytic conditions. The formation of the $Fe^{III}-NH_2$ intermediate (at 0.4 V) in the electrochemical studies

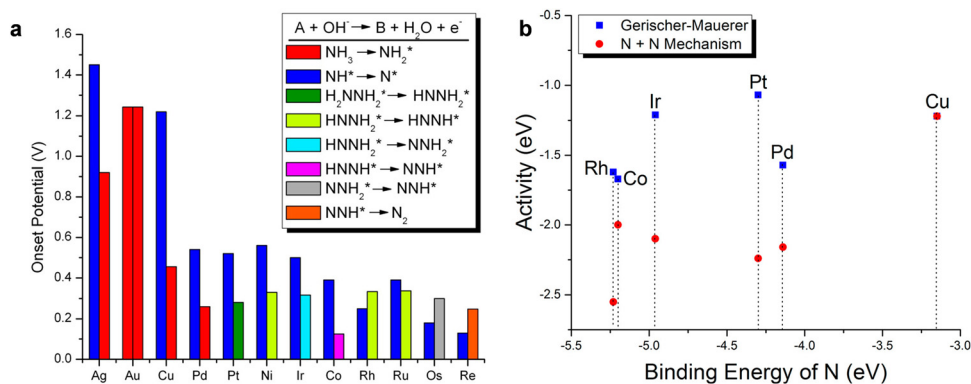


Fig. 5 (a) Onset potential investigation for different transition metals. (b) The AOR activity predicted by both mechanisms. Reproduced with permission from ref. 83 Copyright 2015, ACS publications.



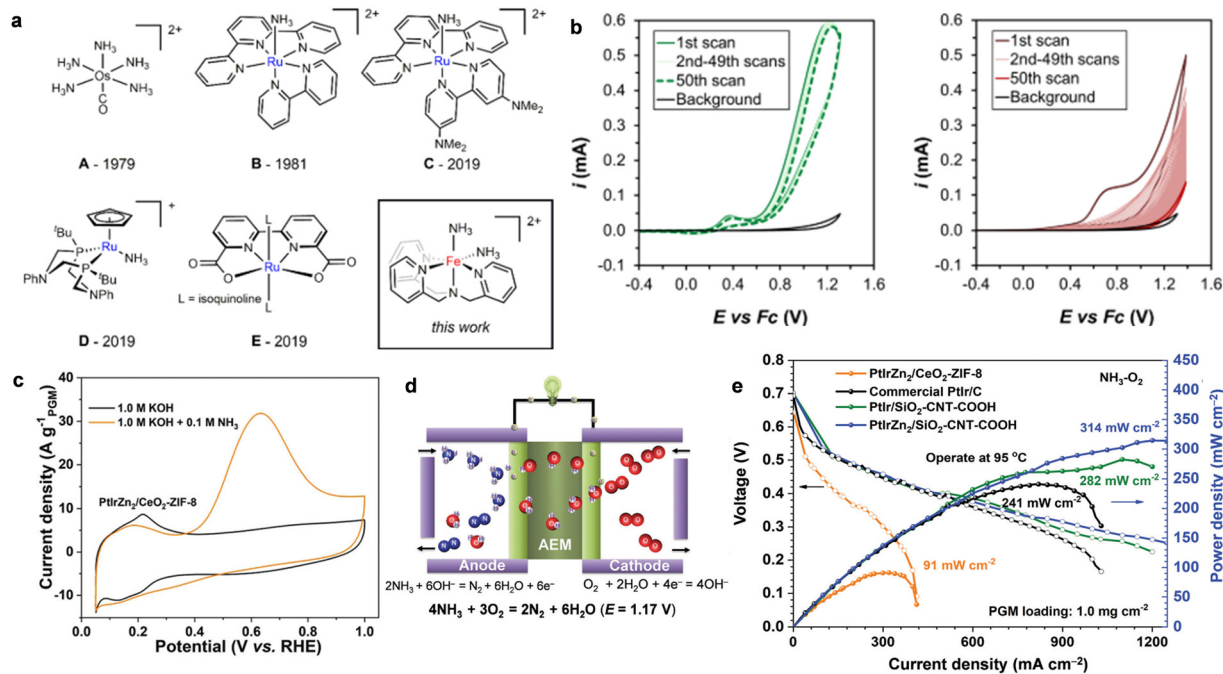


Fig. 6 (a) Representative molecular complexes that catalyze the AOR. (b) The cycling of 2.5 mM [(TPA)Fe(MeCN)₂]OTf₂ (left) or 2.5 mM FeOTf₂ (right) in CH₃CN + 50 mM NH₃ or CH₃CN + 50 mM NH₄OTf solution. Reproduced with permission from ref. 84 Copyright 2019, ACS publications. (c) CV curves of the AOR activity of PtIrZn₂/CeO₂-ZIF-8 in the presence and absence of NH₃. (d) A schematic view of the DAFC single cell. (e) The polarization curves and power density curves of DAFCs with different anode catalysts. Reproduced with permission from ref. 38 Copyright 2020, The Royal Society of Chemistry.

indicated that N–N bond formation facilitates the reaction process. Based on the above-mentioned strategies, molecular electrocatalysts for AOR show great prospects.

4.2.2. PGM-related electrocatalysts. In heterogeneous electrocatalysts, Pt is the most active metal electrocatalyst for AOR to N₂, accompanied by an overpotential of >0.4 V on the surface of polycrystalline Pt.^{34,88} It was demonstrated that a single-crystal Pt electrode, the (100)-type surface was the dominant active site.⁸⁹ Additionally, the Pt surface is deactivated by the strong adsorbing reaction intermediate, such as N_{ad} and NO_{ad} at above 0.6 V, indicating that a higher overpotential can drive a higher AOR rate. Alloying Pt with Ir can effectively lower the onset potential towards N₂ with an increase in temperature (>80 °C),² in which the formation of *N intermediates can occur at a relatively low overpotential with a high reaction rate for a kinetically favorable AOR.⁹⁰ However, Ir is more expensive and scarce than other Pt group metals, and hence exploring Pt-based alloys with earth-abundant elements can be a viable way to minimize the utilization of Ir and enhance the AOR activity and durability. For instance, Wu *et al.* reported the preparation of ternary PtIrZn alloys (~2 nm in particle size) that were highly dispersed on binary CeO₂ and ZIF-8-derived N-doped carbon substrates (PtIrZn/CeO₂-ZIF-8),³⁸ as shown in Fig. 6c. The as-fabricated catalysts showed high AOR activity with an onset potential of 0.35 V, which is lower than that of PtIr/C (0.43 V) in alkaline media. The DFT calculations suggested that doping of Zn in PtIr alloys can facilitate the stronger *NH₃ adsorption than *H adsorption, thereby kinetically triggering AOR with high performance. When PtIrZn/CeO₂-ZIF-8 was used

as the anodic catalyst in an AEM-DAFC (Fig. 6d and e), the peak power density was 91 mW cm⁻². Additionally, when PtIrZn alloys were fabricated on binary substrates composed of SiO₂ with a large surface and conductive CNT-COOH (PtIrZn/SiO₂-CNT-COOH), the anode catalyst reached a remarkable peak power density of 314 mW cm⁻² as a result of the decreased charge transfer resistance and increased mass transport. Thus, the successful alloying strategies show great promise for the exploration of more Pt-based ternary, quaternary alloys with enhanced catalytic activity for AOR.

4.2.3. Non-precious metal-related electrocatalysts. The possibility of using noble-metal free electrocatalysts in an alkaline operating environment is one of their most important advantages. PGM-related AOR catalysts are the most widely studied and intensively reviewed.^{91,92} However, the utilization of PGM-related catalysts is limited due to their high-cost, scarcity and instability. Recently, Ni-related PGM-free catalysts have been demonstrated as promising alternatives to PGMs given that they are more affordable and have higher intrinsic AOR activity. For example, Ni is predicted to exhibit a low onset potential of 0.33 V vs. RHE for AOR. However, the strong Ni–N bonding leads to a high energy barrier of 1.39 eV for the formation of hydrazine species.⁸³ Generally, pure Ni metal delivers poor activity for AOR; however, the activated species such as Ni(OH)₂ layer and NiOOH were demonstrated to be responsible for AOR.^{93,94} Presently, Ni-based catalysts are often restrained by their easy corrosion, which can severely degrade the overall efficiency. Thus, to overcome this limitation, alloying Ni with metals possessing high AOR activity but low affinity



for N is a promising pathway. In this case, Cu is a typical metal with a low Cu–N binding strength, which can effectively enhance the AOR activity due to the increment in active sites.^{95,96} For instance, Xu *et al.* reported the synthesis of NiCu layered hydroxide (LH) nanowires grown directly on carbon cloth *via* the hydrothermal method.⁹⁶ As shown in Fig. 7a, both Ni(OH)₂ and Ni_{0.8}Cu_{0.2} LHs showed approximate onset potentials, which were mainly caused by the generation of NiOOH and Ni_{0.8}Cu_{0.2}OOH, respectively. Interestingly, the current density of the Ni_{0.8}Cu_{0.2} LHs increased sharply in potential regions above the onset potential, manifesting their higher AOR activity than Ni(OH)₂. Moreover, the chronoamperometry tests, as shown in Fig. 7b, demonstrated that the current density of Ni_{0.8}Cu_{0.2} LHs increased to $\sim 35 \text{ mA cm}^{-2}$ by a factor of 6 times, further confirming the significant enhancement in AOR activity by Cu doping. It was also demonstrated that the concentration of NH₃ had a great effect on the AOR activity of Ni_{0.8}Cu_{0.2} LHs, as shown in Fig. 7c. The AOR current was found to gradually increase upon the step-wise injection of NH₃, demonstrating that the Ni_{0.8}Cu_{0.2} LHs still showed activity at high NH₃ concentrations. Intriguingly, the increase in current was slowed down when the NH₃ concentration was higher than 130 mM, which was probably caused by the saturation of the active sites on the surface of Ni_{0.8}Cu_{0.2} LHs. In this work, the choice of doping elements was further studied. The AOR activity of five bimetal NiM LHs (M = Co, Fe, Zn, Mn, Cr) was compared but negligible AOR activity was detected for all five catalysts.

MAFCs have been widely studied to remove NH₃ in wastewater, as noted above. However, the main performance parameters of an

MAFC, such as maximum power density and NH₃ removal efficiency, are random in practical applications because of the deterioration of the catalyst and biofouling. Hence, Tao *et al.* reported the fabrication of an AEM-DAFC, integrating an α -MnO₂/C cathode and NiCu/C anode for the treatment of NH₃-rich wastewater.⁹⁷ The schematic process is shown in Fig. 7d. Additionally, the leachate was collected to evaluate the application of the AEM-DAFC. It was expected that NH₃ can be effectively removed from the leachate as well as electricity is produced from the fuel cell as a bonus. As expected, the open circuit voltage (OCV) increased with an increase in the NH₃ concentration (Fig. 7e). The maximum power density was as high as 0.35 mW cm^{-2} when the NH₃ concentration was 3 M (Fig. 7f). Moreover, a power density of 0.11 mW cm^{-2} was obtained for real wastewater containing $\sim 0.12 \text{ M NH}_3$, indicating its very promising application.

5. Oxygen reduction reaction (ORR)

5.1. Mechanism understanding for ORR

ORR involves two reaction pathways in alkaline media, *i.e.*, $2e^-$ (HO₂⁻) and $4e^-$ (OH⁻) reduction, and their adsorption mode, activation and cleavage barrier on the surface of the catalyst comprehensively determine the activity.^{98,99} Between them, $2e^-$ reduction is not thermodynamically favorable for fuel cells, and some reviews have made insightful summaries for this important reaction,^{100–102} and thus it will not be introduced in this review. Generally, the $4e^-$ ORR process in the alkaline media is as follows:



Fig. 7 (a) CV of Ni_{0.8}Cu_{0.2} LHs and bare Ni(OH)₂ in NH₃-containing electrolyte. (b) The chronoamperometry curves of Ni_{0.8}Cu_{0.2} LHs and bare Ni(OH)₂ with and without NH₃. (c) The current response of Ni_{0.8}Cu_{0.2} LHs to injection of NH₄Cl solution. Reproduced with permission from ref. 96 Copyright 2017, Elsevier. (d) A schematic process of the AEM-DAFC device. (e) The *I*–*V* curves and (f) power density of an AEM-DAFC at different ammonia concentrations using the MnO₂/C cathode and NiCu/C anode at room temperature. Reproduced with permission from ref. 97 Copyright 2020, ACS Publications.



been widely reported due to the good scaling between *OOH and *OH, as shown in Fig. 8b.¹¹³ The U_L as a function of the adsorption of OH free energy can be defined as follows:

$$U_{L1} = -\Delta G_{OH} + 1.72 \quad (5.7)$$

$$U_{L2} = -\Delta G_{OH} + 3.3 \quad (5.8)$$

$$U_{L3} = -\Delta G_{OH} \quad (5.9)$$

$$U_{L4} = -\Delta G_{OH} \quad (5.10)$$

According to the above-mentioned equations, the U_{L1-L4} lines of the four basic steps in Fig. 8c are obtained. The lowest limit potential of the catalytic reaction determines the limit potential of the entire reaction, as represented by solid blue and green lines. For metals with strong binding *OH, *OH \rightarrow H₂O is the potential limit, while the activation of O₂ \rightarrow *OOH is the potential limit for weak binding metals. Undoubtedly, Pt is located at the top of the limit potential volcano.¹¹⁴ Moreover, the analysis has been used to explain the structural sensitivity of ORR. Given that other dense

transition metal sections are roughly arranged along the (111) *OOH vs. *OH scale lines, they are described by the one-dimensional volcanoes in Fig. 8c. The *OH bond on the (211) face on the terrace is stronger (more negative ΔG_{OH}) than on the (111) terrace. For example, although Pt (111) exhibits an excellent ORR performance, strong binding at (211) leads to surface adsorbed *OH poisoning (Fig. 8c). This explains the reduced performance of Pt particles with a smaller size, given that smaller particle sizes can result in more devitalized step sites.¹¹⁵ Alternatively, the step can increase activity and may require smaller particle sizes for catalysts on the weakly bound side.¹¹⁶

5.2. Electrocatalysts for ORR

AEMFCs show many advantages compared to PEMFCs, for example, wider choices for bipolar plates and more enhanced ORR kinetics in alkaline media than in acid media. Particularly, due to their enhanced kinetics, it is expected that PGM-free catalysts can be utilized. Hence, in this part, PGM-based catalysts will not be introduced. Table 3 presents a comparison

Table 3 A comparison of H₂-O₂ or H₂-air AEMFC performance of PGM-free ORR catalysts

ORR catalysts	P_{max} (mW cm ⁻²)	Current density (mA cm ⁻²)	Membrane	Test conditions	Ref.
ZnNC	503 (air)	140 (air)	PAP-TP-85	80 °C, 100% RH, 150 kPa	<i>Angew. Chem., Int. Ed.</i> 2023, 62 , e202216041. ¹²⁵
FeCo-NCH	569 (O ₂); 299.3 (air)	~ 85/0.9 V (O ₂); < 150/0.8 V (air)	PAP-TP-85	80 °C, 200 kPa, 100% RH	<i>Nat. Commun.</i> 2023, 14 , 1822. ¹⁷⁰
NDPC-1000	913 (O ₂); 597 (air)	261/0.8 V (O ₂); ~ 125/0.8 V (air)	PAP-TP-85	80 °C, 2.5 kPa	<i>Adv. Energy Mater.</i> 2023, 13 , 2204390. ¹⁷¹
FeCu-NC	1090 (O ₂); 660 (air)	574/0.8 V (O ₂); 282 (air)	Alkymer W-25	80 °C, 150 kPa, 100% RH	<i>Adv. Energy Mater.</i> 2023, 2302719. ¹⁷²
Ni ₃ N ZrN	151 (air)	~ 50 (air)	Alkymer [®] W-25	90 °C, 200 kPa	<i>Nano Lett.</i> 2023, 23 , 107. ¹⁵⁹
HT-FeCu porphyrrole	510 (O ₂);	~ 85/0.8 V (O ₂)	Versogen, PiperION-A-20HCO ₃	80 °C	<i>ACS Catal.</i> 2023, 13 , 11012. ¹⁷³
CO _{NP} /CNH _{8.1%} NH ₃	619 (O ₂)	880/0.6 V (O ₂)	FAA-3-50	60 °C	<i>Appl. Catal. B Environ.</i> 2023, 323 , 122172. ¹⁷⁴
MnCo ₂ O ₄	310 (air)	~ 120 (air)	PAP-TP-85	95 °C, 250 kPa	<i>Nat. Mater.</i> 2022, 21 , 804. ²³
o-MQFe10 : 20:5	407.5 (O ₂)	290/0.6 V (O ₂)	Tokuyama A201	80 °C, 150 kPa, 100% RH	<i>Angew. Chem., Int. Ed.</i> 2022, 61 , e202117617. ¹⁷⁵
Cu-N-C/GC	324 (O ₂)	~ 75/0.8 V (O ₂)	aQAPS-S 8	60 °C, 200kPa, 100% RH	<i>Angew. Chem., Int. Ed.</i> 2022, 61 , e202211098. ¹⁷⁶
Co ₃ N/C	700 (O ₂)	~ 125/0.8 V (O ₂)	QAPPT	80 °C, 200kPa, 100% R	<i>Sci. Adv.</i> 2022, 8 , 1584. ¹⁷⁷
FPD-Co	654 (O ₂); 323 (air)	760/0.6 V (O ₂); ~ 40/0.8 V (air)	PTFE	80 °C, 100% RH, 200 kPa	<i>Proc. Natl. Acad. Sci. U. S. A.</i> 2022, 119 , e2214089119. ¹⁷⁸
FeCoNCMgOAc	920 (O ₂)	200/0.8 V (O ₂)	Radiation-grafted LDPE	55 °C	<i>ACS Catal.</i> 2022, 12 , 14050. ¹⁷⁹
Fe-Mn-N-C	1320 (O ₂); 605 (air)	1200/0.65 V (O ₂);	PAP-TP-85	80 °C, 100% RH, 250 kPa	<i>Appl. Catal. B Environ.</i> 2022, 317 , 121770. ¹⁸⁰
Ag _{NPs} @Fe-N-C	848 (O ₂); 404 (air)	~ 250/0.8 V (O ₂); < 125/0.8 V (air)	PAP-TP-85	80 °C, 100% RH, 200 kPa	<i>Nano Energy</i> 2022, 100 , 107466. ¹²⁴
CoTPyP@ImRGO	528 (O ₂)	461/0.6 V (O ₂)	alkaline polymer membrane	80 °C, 200 kPa	<i>Nano Energy</i> 2022, 101 , 107565. ¹⁸¹
O-Fe ₄ N ₄ -C	540 (air)	~ 125 (air)	PAP-TP-85	80 °C, 100% RH, 200 kPa	<i>Chem Catal.</i> 2022, 2 , 2750. ¹⁸²
Fe-N-C	2050 (O ₂); 1010 (air)	920/0.8 V (O ₂); 130/0.8 V (air)	HDPE	80 °C, 100% RH, 200 kPa	<i>Nat. Energy</i> 2021, 6 , 834. ¹²³
PF-TMPPCo	226 (O ₂)	250/0.6 V (O ₂)	HDPE-25 μm	60 °C, 0 kPa, 75% RH	<i>Angew. Chem., Int. Ed.</i> 2021, 60 , 4049. ¹³⁴
Fe ²⁺ @NCS-A	~ 108 (O ₂)	~ 12.5/0.8 V (O ₂)	Radiation-grafted LDPE	60 °C, 0 kPa, 100% RH	<i>Adv. Funct. Mater.</i> 2021, 31 , 2102974. ¹⁸³
HT800-FeP	580 (O ₂)	125/0.8 V (O ₂)	ETFE-BTMA	80 °C, 100 kPa	<i>Adv. Funct. Mater.</i> 2021, 31 , 2100963. ¹⁸⁴
Fe-N-C	1440 (O ₂)	~ 250/0.8 V (O ₂)	Not given	65 °C	<i>ACS Catal.</i> 2020, 10 , 225-234. ¹⁸⁵
N-C-CoOx	1050 (O ₂); 660 (air)	290/0.8 V (O ₂); 80/0.8 V (air)	LDPE-BTMA	65 °C, 100% RH, 80 kPa	<i>Angew. Chem., Int. Ed.</i> 2019, 58 , 1046-1051. ¹⁸⁶



of the performance of H_2 - O_2 or H_2 -air AEMFCs consisting of PGM-free ORR catalysts.

5.2.1. Pyrolyzed carbon-based ORR catalysts. Since Jasinsky *et al.* found that the macrocyclic compound phthalocyanine cobalt had good ORR activity in 1964,¹¹⁷ intense studies on the replacement of PGM catalysts by transition metal (TM) materials as ORR catalysts have been carried out. Nevertheless, the high cost of macrocyclic compounds hinders their extensive utilization. In 1989, Yeager *et al.* proposed a model in which electronically conductive surfaces with N-groups can couple with TM metals to form TM-N_x structures by finely selecting appropriate TM, N, and carbon precursors.¹¹⁸ This model offers an effective and economical way to fabricate catalysts by thermal treatment of iron salts and N- and C-containing precursors. At present, the ORR activity of M-N-C catalysts is close to or even outperforms PGMs in alkaline media.

M-N-C catalysts, as the most viable alternatives to PGMs, have attracted significant attention because of their low cost and high intrinsic ORR activity. In particular, many researchers are committed to exploring low-cost and efficient ORR catalysts with the fast development of atomically dispersed catalysts (ADCs). Generally, the state-of-the-art Fe-N-C catalysts have delivered $E_{1/2}$ potentials as high as 0.85 V in alkaline media, which are comparable to commercial Pt/C.^{7,119,120} Various strategies of synthesizing M-N-C-based ADCs and their application in PEMFCs or zinc-air batteries have been reviewed.^{11,121,122} However, when Fe-N-C ORR catalysts are integrated in the AEMFCs, they show a poor performance compared with Pt/C cathodes because of the inefficient mass transport and low catalyst loading. Thus, to address this problem, Mustain *et al.* developed the utilization of a commercial Fe-N-C catalyst with single-atom Fe-N_x sites in the AEMFC

cathode.¹²³ The Fe-N-C catalysts were further modified by increasing their average pore size to facilitate the efficient transport of generated H_2O on the anode side in the CLs, as well as increasing the graphitization of the catalyst to decrease the hydrophilicity (Fig. 9a). The average pore size was increased by mixing amorphous fumed SiO_2 with Fe metal salt and NC precursors, followed by high-temperature pyrolysis. Upon removing the SiO_2 template, the final desired Fe-N-C catalyst was obtained by a second pyrolysis to increase the degree of graphitization. The as-prepared Fe-N-C catalyst showed a high $E_{1/2}$ of 0.846 V, which is comparable to Pt/C at different rotating rates in the rate of 400–2500 r.p.m (Fig. 9b). Additionally, it was found that water management played important roles to guarantee the high-performance and durability, as shown in Fig. 9c. When the cell was operated under high water accumulation at the anode (anode/cathode/cell temperature: 60/60/60 °C) with full humidity, the cell performance was low. Once the cell temperature was evaluated at 70 °C, the peak power density correspondingly increased. Additionally, applying backpressure to the cathode could also significantly increase the cell performance, while it shows the opposite effect for the anode side, as shown in Fig. 9c (blue curve).

Although Fe-N-C shows higher ORR activity than commercial Pt/C in alkaline media, Fe-N-C catalysts often suffer from the unsatisfactory stability because the Fe^{2+} intermediates tend to generate the Fenton effect, which impairs the active sites and the polymer membrane. To enhance the stability of Fe-N-C for ORR, Cao *et al.* developed an $Ag_{NP}@Fe-N-C$ composite catalyst, showing an efficient ORR performance and robust stability.¹²⁴ After assembling an AFMFC, the catalyst showed extremely high peak power density (0.848 $W\ cm^{-2}$) and long-term device durability of 200 h in an H_2 /air (CO_2 -free) system. Later, they reported the synthesis of a ZnNC catalyst, which showed

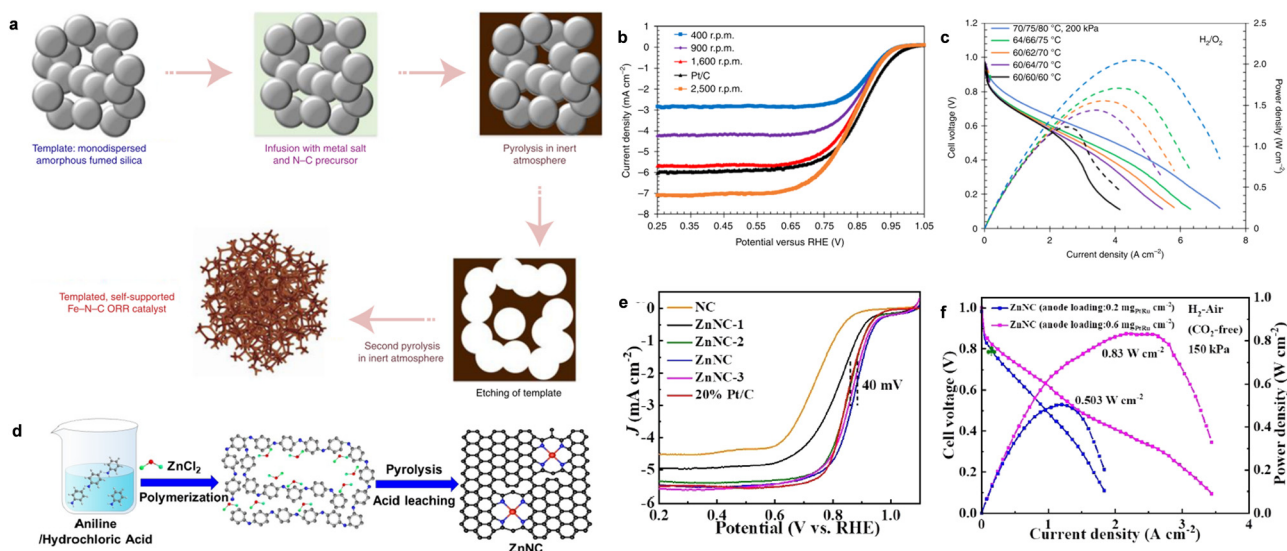


Fig. 9 (a) The synthesis of the desired structure of the Fe-N-C catalyst. (b) The ORR LSV curves of Fe-N-C at different rotating rates compared to Pt/C. (c) The H_2 - O_2 AEM performance of the Fe-N-C cathode. The curves were obtained with $1\ mg\ cm^{-2}$ Fe-N-C as the cathode and $0.6\ mg\ cm^{-2}$ PtRu as the anode. Reproduced with permission from ref. 123 Copyright 2021, Nature Publications. (d) The synthesis of ZnNC. (e) The LSV curves of ZnNC with different reference catalysts. (f) The polarization and power density curves of H_2 -air (CO_2 -free) AEMFC with ZnNC in the cathode and PtRu/C in the anode. Reproduced with permission from ref. 125 Copyright 2022, Wiley-VCH GmbH Publications.





Fig. 10 (a) The advantage of catalyst layer based on homogeneous catalysis using the TMPPCo catalyst. (b) The LSV curves of PF-TMPPCo and the compared catalysts in 0.1 M KOH solution. (c) H_2 - O_2 AEMFC performance comparison. Reproduced with permission from ref. 134 Copyright 2020, Wiley-VCH GmbH Publications. (d) The strategies for molecular catalysts to heterogeneous catalysts. (e) The LSV curves of 1-ZIF-67 and the compared catalysts in 0.1 M KOH solution. Reproduced with permission from ref. 139 Copyright 2021, Wiley-VCH GmbH Publications. (f) The top views of the optimized structures of Co@rhM-PorBTD (up) and Co@sql-PorBTD (down) with eclipsed (AA) structure. (g) ORR LSV curves of Co@rhM-PorBTD , Co@sql-PorBTD and Pt/C catalysts. Reproduced with permission from ref. 145 Copyright 2023, ACS Publications.

surface areas (up to $4200 \text{ m}^2 \text{ g}^{-1}$), flexible pore size ($\sim 5.0 \text{ nm}$), robust thermal stability ($\sim 600 \text{ }^\circ\text{C}$) and high charge mobility ($\sim 8.1 \text{ cm}^2 \text{ V}^{-1} \text{ s}^{-1}$).¹⁴² Hence, COPs have also attracted intense interest due to their promising potential applications for oxygen reduction. COPs can not only strongly tailor the incorporation of heteroatoms and locations of active sites, but also supply C/N atoms in the ligands with sufficient flexibility to implant efficient metals into the structure. Additionally, the well-designed COPs with ideal pore size and good stability favor of the electrocatalytic processes in a direct way. However, COPs show mediocre activity compared with the conventional metal-based ORR catalysts due to the constrained electrical conductivity.¹⁴³ Combining conductive materials (carbon nanotubes, graphene, *etc.*) or mixing conductive carbon (acetylene black, *etc.*) with COPs is a promising method to improve the conductivity of COP-related ORR catalysts. For instance, Xiang *et al.* reported the preparation of a pyrolysis-free Fe-COF hybrid catalyst self-assembled with graphene *via* van der Waals interaction.¹⁴⁴ The *pfSAC-Fe* hybrids exhibited impressive ORR activity due to the synergistic effect between the active

COPs and conductive graphene. Moreover, Echegoyen *et al.* reported the synthesis of two types of Co(II)-porphyrin/[2,1,3]-benzothiadiazole (BTD)-based covalent organic frameworks (Fig. 10f, COFs; Co@rhM-PorBTD and Co@sql-PorBTD), which showed excellent ORR activity.¹⁴⁵ Moreover, the ORR LSV curves demonstrated that these two COFs showed comparable ORR activity and outperformed the mass activity of Pt/C (20%) by 5.8 times for Co@rhM-PorBTD and 1.3 times for Co@sql-PorBTD (Fig. 10g).

5.2.3. Metal oxide and related hybrid ORR catalysts. In recent years, transition metal mixed oxides including monometallic oxides, perovskite oxides and spinel oxides have been widely used as ORR catalysts.^{5,6,146,147} In particular, perovskite metal oxides have shown great promise for high ORR performance because of their robust crystal structure, high conductivity and rich defects. Recently, versatile perovskite oxides have exhibited high ORR activity.^{5,148–151} For instance, Weidner *et al.* reported the preparation of LaCoO_3 fibers for ORR by the electrospinning strategy. The as-obtained LaCoO_3 fibers exhibited a much higher ORR performance due to the abundant



active sites compared with LaCoO_3 powder.¹⁵² Additionally, doping cations or anions is an efficient method to improve the intrinsic activity of catalysts by modulating their electronic structural energy, electronic band structure and oxygen vacancies.^{5,153,154} For example, Ramakrishna *et al.* prepared S-doped CaMnO_3 (CMO/S) nanotubes by electrospinning and subsequent thermal treatment with S power.¹⁵¹ The unique microstructure could significantly facilitate the diffusion of oxygen inside and outside the catalyst during the ORR process. Additionally, the incorporation of S could also increase the electric conductivity and vacancy defects in CaMnO_3 , thereby optimizing the ORR activity of CMO/S. In electrochemical reactions, individual perovskites are relatively limited in regulating the surface electronic states and intermediate adsorption energies. Therefore, the fabrication of perovskite-containing heterostructures with a strong interfacial effect has become one of the effective strategies to enhance the activity of perovskite materials. For instance, Liu *et al.* reported the enhanced ORR performance of hetero-structured $\text{SMO}_x\text{-SMO}$ synthesized *via* epitaxial growth.⁵ The synthesis process is shown in Fig. 11a. It should be noted that $\text{SMO}_x\text{-SMO}$ and $\text{SMO}_x\text{-MO}$ with different interfaces were obtained by varying the molar ratio of Sr^{2+} and Mn^{2+} . As shown in Fig. 11b and c, $\text{SMO}_x\text{-SMO}$ showed superior ORR activity with $E_{1/2} = 0.74$ V and j of 5.46 mA cm^{-2} at 0.2 V, which was much better than that of $\text{SMO}_x\text{-MO}$ ($E_{1/2} = 0.67$ V and j of 5.46 mA cm^{-2} at 0.2 V). According to the simulated results, the epitaxial growth hetero-junction of $\text{SMO}_x\text{-SMO}$ has a more stable thermodynamic structure than non-epitaxial growth of $\text{SMO}_x\text{-SMO}$ due to the

lower formation energy of the former. Also, the positive shift in the Mn band center could enhance the Mn oxidation state, while the partial filling of e_g could significantly optimize the adsorption of intermediate $^*\text{OH}$ to improve the activity of $\text{SMO}_x\text{-SMO}$.

Moreover, the strong scaling relationship of adsorption energy between ORR intermediates gives the minimum theoretical overpotential ($\sim 0.3\text{-}0.4$ V) for a single site, which causes unsatisfactory activity. Hence, constructing a single-site pair-based active site on metal oxides can probably break the limit of the adsorption-energy scale relationship to improve the ORR performance by modulating the spin-state to optimize the adsorption energy. For example, Zou *et al.* developed a Pt-Fe pair by implanting Pt atomic sites on $\alpha\text{-Fe}_2\text{O}_3$ (012) facets and the as-fabricated $\text{Pt}_1\text{-Fe/Fe}_2\text{O}_3$ (012) catalyst delivered a record onset and $E_{1/2}$ of 1.15 and 1.05 V, respectively. The STEM image clearly displayed the individual platinum atoms dispersed on the surface of Fe_2O_3 and the line intensity plot further verified the existence of Pt-Fe pairs. The predicted DFT calculations showed that the d-band of Fe can well match the d-band of Pt, facilitating strong electronic coupling in the Pt-Fe pair. In particular, for $\text{Pt}_1\text{-Fe/Fe}_2\text{O}_3$ (012), the electron coupling gives Pt a partially occupied d_z^2 near the Fermi level, which can maximize the frontier orbital overlapping. The formed Sigma bonds potentially provide active sites for O_2 adsorption and activation. In addition, considering the transfer of electrons from Fe to Pt, the original completely occupied e_g orbital of high-spin Fe^{3+} became a partially occupied state, which also favored O_2 adsorption. As expected, the ORR polarization curves

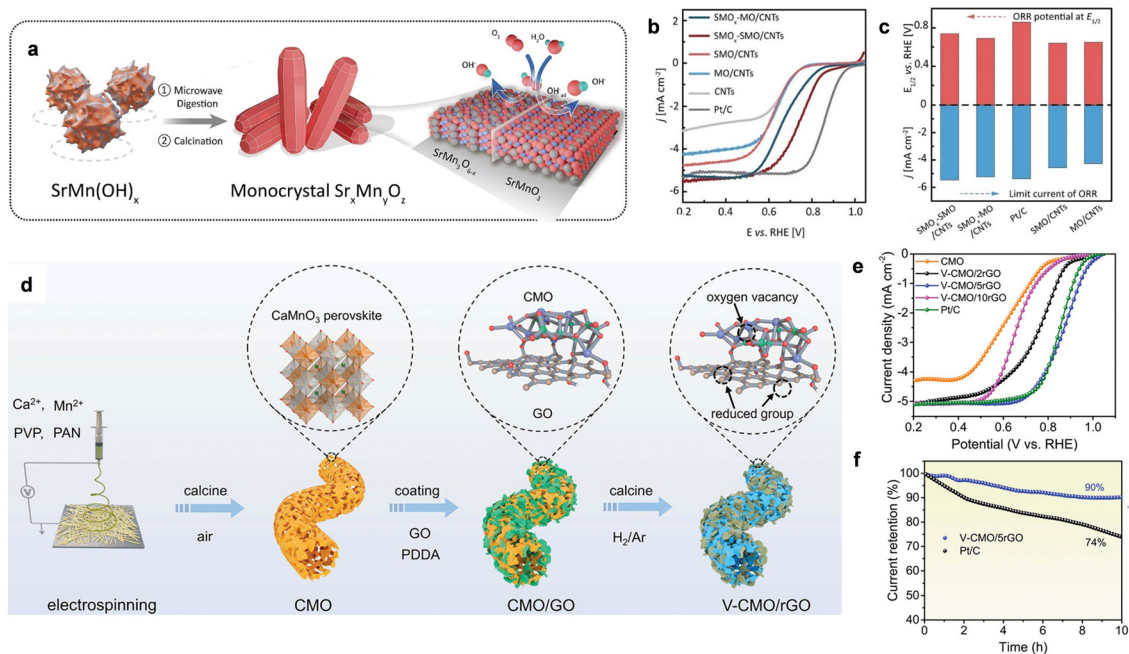


Fig. 11 (a) The synthesis scheme of $\text{SMO}_x\text{-SMO}$. (b) The LSV curves of ORR using different catalysts in 0.1 M KOH solution. (c) A comparison of $E_{1/2}$ and the limit current density for the related catalysts. Reproduced with permission from ref. 5 Copyright 2021, Wiley-VCH GmbH Publications. (d) The synthesis process of V-CMO/rGO. (e) ORR polarization curves for V-CMO/rGO and related reference catalysts. (f) The stability tests of V-CMO/rGO and Pt/C catalysts. Reproduced with permission from ref. 155 Copyright 2023, Wiley-VCH GmbH Publications.



showed that Pt₁-Fe/Fe₂O₃ (012) exhibited the highest performance, delivering an extremely high onset potential of 1.15 V, the highest mass activity of 14.9 A mg_{Pt}⁻¹ at 0.95 V among the investigated catalysts and robust stability for ORR. The mechanism suggested that the enhanced ORR kinetics was dramatically caused by the facile O₂ activation on the Pt-Fe pair and OH* desorption on the Pt single-site. Thus, the optimized O₂ activation and OH* desorption could overcome the scaling relationships, which could not be optimized on the catalyst per unit point.

Modifying metal oxides with rich oxygen defects has been considered an efficient strategy to design ORR catalysts with high activity. Peng *et al.* developed porous CaMnO₃ (CMO) nanofibers modified with rich vacancies and reduced graphene oxide (V-CMO/rGO) as efficient ORR catalysts.¹⁵⁵ V-CMO/rGO was prepared *via* a facile electrospinning method and subsequent electrostatic adsorption of GO with appropriate thermal treatment in air, as shown in Fig. 11d. CMO covered with uniform rGO was obtained by altering the adsorbent amount of GO. Moreover, the final V-CMO/rGO with well-designed 3D framework could not only enhance the exposed active sites, but also increase the electrical conductivity. In particular, the $E_{1/2}$ of V-CMO/5rGO was much higher than that of Pt/C, V-CMO/2rGO and V-CMO/10rGO, as displayed in Fig. 11e. All the CMO catalysts showed superior ORR activity to pure V-CMO because of the highly conductive rGO. The chronoamperometry measurement for the stability test in Fig. 11f verified that V-CMO/5rGO retained better durability than Pt/C. The DFT results demonstrated that CMO as the main active species showed very poor activity for ORR as rGO. Also, Mn was selected as the active site

for the 4e⁻ ORR pathway. The excellent performance could stem from the modulation of the oxygen vacancies on the Mn active site, as well as the accelerated electron transfer induced by the uniformly distributed rGO.

6. Summary and perspectives

The importance of the “hydrogen economy” and “ammonia economy” in the modern society cannot be overstated due to their high energy density and carbon neutral nature in the future energy landscape. In the case of AEMFCs, we believe there is still a lot of room for further exploration. Therefore, increasing efforts are a very desirable contribution to this promising area, especially for catalysts. In the past few decades, important research progress has been made in the development of non-precious catalysts for AEMFCs. However, their catalytic activity still does not reach the that of PGMs. For practical application in AEMFCs, the large-scale development of well-structured and cost-effective catalysts is a prerequisite. The future direction of development for catalysts and key challenges for AEMFCs are summarized in Fig. 12, which also properly addresses the comprehensive challenges that require cooperation between industry and academia. It is believed that AEMFC technology will open up a new path for the development of the next generation of energy-conversion devices to meet the growing energy needs of modern society.

6.1. Catalyst screening

Exploring efficient and robust HOR/AOR/ORR non-PGM catalysts that can match or exceed the performance benchmark of

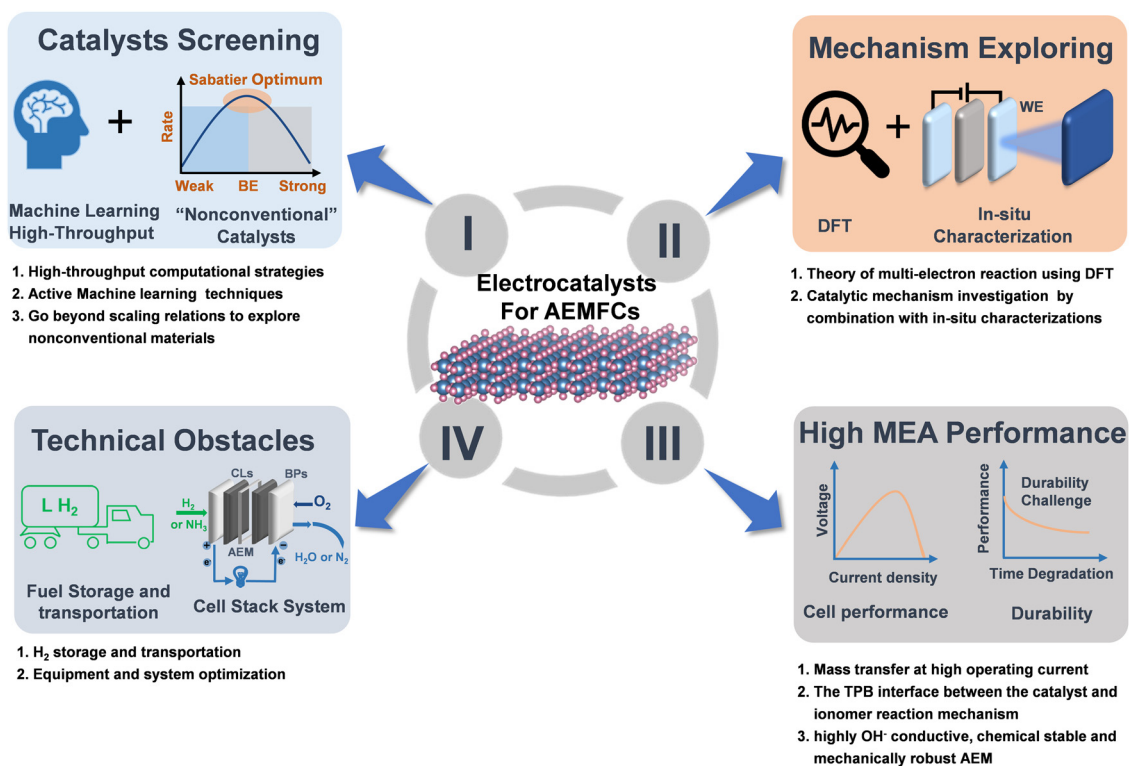


Fig. 12 A schematic of future developments of electrocatalysts for AEMFCs and remaining technological challenges.



PGMs is crucial. Although the excellent performance of TM-based materials has been reported, a great deal of studies still need to be done on this topic. On one hand, exploring new materials through high-throughput computation and active machine learning strategies can greatly accelerate the development in the field.^{156,157} On the other hand, the dedicated research for non-traditional materials or structures that inherently outperform the “standard” scaling relations can help to design and explore the next generation of efficient catalysts.

6.2. Mechanism exploring

Versatile types of catalysts have been designed for efficient HOR, AOR and ORR; nevertheless, a systematic deep mechanistic understanding of the reactions in alkaline media is still lacking, especially for AOR. Presently, most AOR catalysts are still prepared by trial and error. Alternatively, it is necessary to develop highly active catalysts for potential applications in AEMFCs by combining computational and experimental approaches, especially advanced *in situ* characterization techniques. For example, *in situ/operando* XAS, TEM and Raman spectroscopy, are highly required for real-time monitoring of the dynamic evolution process of the catalyst structure. Also, systematic studies can greatly facilitate an in-depth understanding of the catalytic mechanism of catalysts and rational design of more novel low-cost and efficient catalysts.

6.3. High MEA performance

At high current densities, mass transfer is a major limiting factor for RDE and integrated MEA device testing. The RDE test uses a thin CL and low catalyst loading to alleviate the mass transfer problem because thin CLs can facilitate the efficient circulation of the electrolyte. Simultaneously, O₂ diffuses easily from thin CLs. In contrast, thick CLs with a high catalyst loading will cause serious mass transfer problems for reactants or products, resulting in large gaps in performance. Thus, to alleviate the mass transfer problem, thin CLs are directly deposited on the membrane and highly porous conductive substrates. The high hydrophobicity of polymer ionomers may limit the electrolyte proximity to the electrode surface, thereby reducing the cell performance. Hence, it is critical to optimize the three-phase boundary (TPB) of the electrode reaction.

Moreover, the surface functional groups of the catalyst, backbone chains of ionomers, polarity of the solvent, *etc.* can also impact the quality of the catalyst ink and probably cause the catalyst to aggregate on the electrode during the manufacturing of MEAs, thereby blocking the mass transfer channel and degrading the cell performance. In particular, even some stable M–N–C materials showing robust stability in the RDE system are subjected to fast degradation under high-temperature operations. Thus, to alleviate the degradation, robust metal oxides are potentially utilized to stabilize carbon-related catalysts for fuel cells.^{38,158} Furthermore, chemically stable, mechanically robust and highly electric conductive AEMs are also urgently required to propel the development of AEMFCs.

6.4. Technical obstacles

Although hydrogen is the most promising fuel due to its simple anodization, its storage and transport are a huge challenge impeding the development of a hydrogen economy. In the case of NH₃, the crossover of ammonia from the anode to cathode *via* AEMs is also a serious challenge. Moreover, the rational design and upgrading of equipment and systems are also highly required to meet the demand of highly safe, low-cost, high-efficiency and facile operability cell stacks under both experimental and practical industry environments.

Conflicts of interest

There are no conflicts to declare.

Acknowledgements

This work was supported by the National Natural Science Foundation of China (No. 22202214, 51825204) and Natural Science Foundation of Liaoning Province-Outstanding Youth Foundation (2022-YQ-02). G. L. thanks the financial support from the New Cornerstone Science Foundation through the XPLOER PRIZE.

References

- 1 F. Jiao and B. Xu, Electrochemical Ammonia Synthesis and Ammonia Fuel Cells, *Adv. Mater.*, 2019, **31**(31), 1805173.
- 2 N. M. Adli, H. Zhang, S. Mukherjee and G. Wu, Review-Ammonia Oxidation Electrocatalysis for Hydrogen Generation and Fuel Cells, *J. Electrochem. Soc.*, 2018, **165**(15), J3130.
- 3 Y. Yang, P. Li, X. Zheng, W. Sun, S. X. Dou, T. Ma and H. Pan, Anion-exchange membrane water electrolyzers and fuel cells, *Chem. Soc. Rev.*, 2022, **51**(23), 9620–9693.
- 4 Y. Yang, C. R. Peltier, R. Zeng, R. Schimmenti, Q. Li, X. Huang, Z. Yan, G. Potsi, R. Selhorst, X. Lu, W. Xu, M. Tader, A. V. Soudackov, H. Zhang, M. Krumov, E. Murray, P. Xu, J. Hitt, L. Xu, H.-Y. Ko, B. G. Ernst, C. Bundschu, A. Luo, D. Markovich, M. Hu, C. He, H. Wang, J. Fang, R. A. DiStasio, L. F. Kourkoutis, A. Singer, K. J. T. Noonan, L. Xiao, L. Zhuang, B. S. Pivovarov, P. Zelenay, E. Herrero, J. M. Feliu, J. Suntivich, E. P. Giannelis, S. Hammes-Schiffer, T. Arias, M. Mavrikakis, T. E. Mallouk, J. D. Brock, D. A. Muller, F. J. DiSalvo, G. W. Coates and H. D. Abruña, Electrocatalysis in Alkaline Media and Alkaline Membrane-Based Energy Technologies, *Chem. Rev.*, 2022, **122**(6), 6117–6321.
- 5 C. Chen, X.-T. Wang, J.-H. Zhong, J. Liu, G. I. N. Waterhouse and Z.-Q. Liu, Epitaxially Grown Heterostructured SrMn₃O_{6-x}-SrMnO₃ with High-Valence Mn^{3+/4+} for Improved Oxygen Reduction Catalysis, *Angew. Chem., Int. Ed.*, 2021, **60**(40), 22043–22050.



- 6 R. Gao, J. Wang, Z.-F. Huang, R. Zhang, W. Wang, L. Pan, J. Zhang, W. Zhu, X. Zhang, C. Shi, J. Lim and J.-J. Zou, Pt/Fe₂O₃ with Pt-Fe pair sites as a catalyst for oxygen reduction with ultralow Pt loading, *Nat. Energy*, 2021, **6**(6), 614–623.
- 7 A. Han, X. Wang, K. Tang, Z. Zhang, C. Ye, K. Kong, H. Hu, L. Zheng, P. Jiang, C. Zhao, Q. Zhang, D. Wang and Y. Li, An Adjacent Atomic Platinum Site Enables Single-Atom Iron with High Oxygen Reduction Reaction Performance, *Angew. Chem., Int. Ed.*, 2021, **60**(35), 19262–19271.
- 8 A. Han, Z. Zhang, X. Li, D. Wang and Y. Li, Atomic Thickness Catalysts: Synthesis and Applications, *Small Methods*, 2020, **4**(9), 2000248.
- 9 A. Han, Z. Zhang, J. Yang, D. Wang and Y. Li, Carbon-Supported Single-Atom Catalysts for Formic Acid Oxidation and Oxygen Reduction Reactions, *Small*, 2021, **17**(16), 2004500.
- 10 Y. Wang, J. Wu, S. Tang, J. Yang, C. Ye, J. Chen, Y. Lei and D. Wang, Synergistic Fe–Se Atom Pairs as Bifunctional Oxygen Electrocatalysts Boost Low-Temperature Rechargeable Zn-Air Battery, *Angew. Chem., Int. Ed.*, 2023, **62**(15), e202219191.
- 11 P. Cui, L. Zhao, Y. Long, L. Dai and C. Hu, Carbon-Based Electrocatalysts for Acidic Oxygen Reduction Reaction, *Angew. Chem., Int. Ed.*, 2023, **62**, e202218269.
- 12 Y. T. Chan, K. Siddharth and M. Shao, Investigation of cubic Pt alloys for ammonia oxidation reaction, *Nano Res.*, 2020, **13**(7), 1920–1927.
- 13 K. Nakajima, H. Toda, K. Sakata and Y. Nishibayashi, Ruthenium-catalysed oxidative conversion of ammonia into dinitrogen, *Nat. Chem.*, 2019, **11**(8), 702–709.
- 14 H. Du, Z. Du, T. Wang, B. Li, S. He, K. Wang, L. Xie, W. Ai and W. Huang, Unlocking Interfacial Electron Transfer of Ruthenium Phosphides by Homologous Core–Shell Design toward Efficient Hydrogen Evolution and Oxidation, *Adv. Mater.*, 2022, **34**(37), 2204624.
- 15 T. Zhao, M. Li, D. Xiao, X. Yang, Q. Li, L. An, Z. Deng, T. Shen, M. Gong, Y. Chen, G. Wang, X. Zhao, L. Xiao, X. Yang, L. Li and D. Wang, Pseudo-Pt Monolayer for Robust Hydrogen Oxidation, *J. Am. Chem. Soc.*, 2023, **145**, 4088–4097.
- 16 Y. Zhou, Z. Xie, J. Jiang, J. Wang, X. Song, Q. He, W. Ding and Z. Wei, Lattice-confined Ru clusters with high CO tolerance and activity for the hydrogen oxidation reaction, *Nat. Catal.*, 2020, **3**(5), 454–462.
- 17 S. Zhu, X. Qin, F. Xiao, S. Yang, Y. Xu, Z. Tan, J. Li, J. Yan, Q. Chen, M. Chen and M. Shao, The role of ruthenium in improving the kinetics of hydrogen oxidation and evolution reactions of platinum, *Nat. Catal.*, 2021, **4**(8), 711–718.
- 18 J. Mao, C.-T. He, J. Pei, Y. Liu, J. Li, W. Chen, D. He, D. Wang and Y. Li, Isolated Ni Atoms Dispersed on Ru Nanosheets: High-Performance Electrocatalysts toward Hydrogen Oxidation Reaction, *Nano Lett.*, 2020, **20**(5), 3442–3448.
- 19 W. Sheng, Z. Zhuang, M. Gao, J. Zheng, J. G. Chen and Y. Yan, Correlating hydrogen oxidation and evolution activity on platinum at different pH with measured hydrogen binding energy, *Nat. Commun.*, 2015, **6**(1), 5848.
- 20 W. Sheng, H. A. Gasteiger and Y. Shao-Horn, Hydrogen Oxidation and Evolution Reaction Kinetics on Platinum: Acid vs Alkaline Electrolytes, *J. Electrochem. Soc.*, 2010, **157**(11), B1529.
- 21 Y. Duan, X.-L. Zhang, F.-Y. Gao, Y. Kong, Y. Duan, X.-T. Yang, X.-X. Yu, Y.-R. Wang, S. Qin, Z. Chen, R. Wu, P.-P. Yang, X.-S. Zheng, J.-F. Zhu, M.-R. Gao, T.-B. Lu, Z.-Y. Yu and S.-H. Yu, Interfacial Engineering of Ni/V₂O₃ Heterostructure Catalyst for Boosting Hydrogen Oxidation Reaction in Alkaline Electrolytes, *Angew. Chem., Int. Ed.*, 2023, **62**(10), e202217275.
- 22 W. Ni, A. Krammer, C.-S. Hsu, H. M. Chen, A. Schüler and X. Hu, Ni₃N as an Active Hydrogen Oxidation Reaction Catalyst in Alkaline Medium, *Angew. Chem., Int. Ed.*, 2019, **58**(22), 7445–7449.
- 23 W. Ni, T. Wang, F. Héroguel, A. Krammer, S. Lee, L. Yao, A. Schüler, J. S. Luterbacher, Y. Yan and X. Hu, An efficient nickel hydrogen oxidation catalyst for hydroxide exchange membrane fuel cells, *Nat. Mater.*, 2022, **21**(7), 804–810.
- 24 M. Wang, H. Yang, J. Shi, Y. Chen, Y. Zhou, L. Wang, S. Di, X. Zhao, J. Zhong, T. Cheng, W. Zhou and Y. Li, Alloying Nickel with Molybdenum Significantly Accelerates Alkaline Hydrogen Electrocatalysis, *Angew. Chem., Int. Ed.*, 2021, **60**(11), 5771–5777.
- 25 F. Yang, X. Bao, P. Li, X. Wang, G. Cheng, S. Chen and W. Luo, Boosting Hydrogen Oxidation Activity of Ni in Alkaline Media through Oxygen-Vacancy-Rich CeO₂/Ni Heterostructures, *Angew. Chem., Int. Ed.*, 2019, **58**(40), 14179–14183.
- 26 T. B. Ferriday and P. H. Middleton, Alkaline fuel cell technology - A review, *Int. J. Hydrogen Energy*, 2021, **46**(35), 18489–18510.
- 27 W. E. Mustain, M. Chatenet, M. Page and Y. S. Kim, Durability challenges of anion exchange membrane fuel cells, *Energy Environ. Sci.*, 2020, **13**(9), 2805–2838.
- 28 J. Zhang, W. Zhu, T. Huang, C. Zheng, Y. Pei, G. Shen, Z. Nie, D. Xiao, Y. Yin and M. D. Guiver, Recent Insights on Catalyst Layers for Anion Exchange Membrane Fuel Cells, *Adv. Sci.*, 2021, **8**(15), 2100284.
- 29 A. Serov, I. V. Zenyuk, C. G. Arges and M. Chatenet, Hot topics in alkaline exchange membrane fuel cells, *J. Power Sources*, 2018, **375**, 149–157.
- 30 D. R. Dekel, Review of cell performance in anion exchange membrane fuel cells, *J. Power Sources*, 2018, **375**, 158–169.
- 31 S. F. Yin, B. Q. Xu, X. P. Zhou and C. T. Au, A mini-review on ammonia decomposition catalysts for on-site generation of hydrogen for fuel cell applications, *Appl. Catal., A*, 2004, **277**(1), 1–9.
- 32 Q. Ma, R. Peng, Y. Lin, J. Gao and G. Meng, A high-performance ammonia-fueled solid oxide fuel cell, *J. Power Sources*, 2006, **161**(1), 95–98.
- 33 Y. Aoki, T. Yamaguchi, S. Kobayashi, D. Kowalski, C. Zhu and H. Habazaki, High-Efficiency Direct Ammonia Fuel Cells Based on BaZr_{0.1}Ce_{0.7}Y_{0.2}O_{3-δ}/Pd Oxide-Metal Junctions, *Glob. Chall.*, 2018, **2**(1), 1700088.



- materials for electrocatalysis, *Nano Energy*, 2020, **70**, 104525.
- 144 P. Peng, L. Shi, F. Huo, C. Mi, X. Wu, S. Zhang and Z. Xiang, A pyrolysis-free path toward superiorly catalytic nitrogen-coordinated single atom, *Sci. Adv.*, 2019, **5**(8), eaaw2322.
- 145 S. Bhunia, A. Peña-Duarte, H. Li, H. Li, M. F. Sanad, P. Saha, M. A. Addicoat, K. Sasaki, T. A. Strom, M. J. Yacamán, C. R. Cabrera, R. Seshadri, S. Bhattacharya, J.-L. Brédas and L. Echegoyen, [2,1,3]-Benzothiadiazole-Spaced Coporphyrin-Based Covalent Organic Frameworks for O₂ Reduction, *ACS Nano*, 2023, **17**(4), 3492–3505.
- 146 N. Heller-Ling, M. Prestat, J. L. Gautier, J. F. Koenig, G. Poillerat and P. Chartier, Oxygen electroreduction mechanism at thin Ni_xCo_{3-x}O₄ spinel films in a double channel electrode flow cell (DCEFC), *Electrochim. Acta*, 1997, **42**(2), 197–202.
- 147 Z. Zhuang, Y. Li, R. Yu, L. Xia, J. Yang, Z. Lang, J. Zhu, J. Huang, J. Wang, Y. Wang, L. Fan, J. Wu, Y. Zhao, D. Wang and Y. Li, Reversely trapping atoms from a perovskite surface for high-performance and durable fuel cell cathodes, *Nat. Catal.*, 2022, **5**(4), 300–310.
- 148 J. Suntivich, H. A. Gasteiger, N. Yabuuchi, H. Nakanishi, J. B. Goodenough and Y. Shao-Horn, Design principles for oxygen-reduction activity on perovskite oxide catalysts for fuel cells and metal–air batteries, *Nat. Chem.*, 2011, **3**(7), 546–550.
- 149 Z. Li, L. Lv, J. Wang, X. Ao, Y. Ruan, D. Zha, G. Hong, Q. Wu, Y. Lan, C. Wang, J. Jiang and M. Liu, Engineering phosphorus-doped LaFeO_{3-δ} perovskite oxide as robust bifunctional oxygen electrocatalysts in alkaline solutions, *Nano Energy*, 2018, **47**, 199–209.
- 150 S. Zhai, H. Xie, P. Cui, D. Guan, J. Wang, S. Zhao, B. Chen, Y. Song, Z. Shao and M. Ni, A combined ionic Lewis acid descriptor and machine-learning approach to prediction of efficient oxygen reduction electrodes for ceramic fuel cells, *Nat. Energy*, 2022, **7**(9), 866–875.
- 151 S. Peng, X. Han, L. Li, S. Chou, D. Ji, H. Huang, Y. Du, J. Liu and S. Ramakrishna, Electronic and Defective Engineering of Electrospun CaMnO₃ Nanotubes for Enhanced Oxygen Electrocatalysis in Rechargeable Zinc–Air Batteries, *Adv. Energy Mater.*, 2018, **8**(22), 1800612.
- 152 J. Shim, K. J. Lopez, H. J. Sun, G. Park, J. C. An, S. Eom, S. Shimpalee and J. W. Weidner, Preparation and characterization of electrospun LaCoO₃ fibers for oxygen reduction and evolution in rechargeable Zn–air batteries, *J. Appl. Electrochem.*, 2015, **45**(9), 1005–1012.
- 153 X. Sun, Y. Guo, C. Wu and Y. Xie, The Hydric Effect in Inorganic Nanomaterials for Nanoelectronics and Energy Applications, *Adv. Mater.*, 2015, **27**(26), 3850–3867.
- 154 A. Han, X. Zhou, X. Wang, S. Liu, Q. Xiong, Q. Zhang, L. Gu, Z. Zhuang, W. Zhang, F. Li, D. Wang, L.-J. Li and Y. Li, One-step synthesis of single-site vanadium substitution in 1T-WS₂ monolayers for enhanced hydrogen evolution catalysis, *Nat. Commun.*, 2021, **12**(1), 709.
- 155 H. Huang, A. Huang, D. Liu, W. Han, C.-H. Kuo, H.-Y. Chen, L. Li, H. Pan and S. Peng, Tailoring Oxygen Reduction Reaction Kinetics on Perovskite Oxides via Oxygen Vacancies for Low-Temperature and Knittable Zinc–Air Batteries, *Adv. Mater.*, 2023, 2303109.
- 156 M. Zhong, K. Tran, Y. Min, C. Wang, Z. Wang, C.-T. Dinh, P. De Luna, Z. Yu, A. S. Rasouli, P. Brodersen, S. Sun, O. Voznyy, C.-S. Tan, M. Askerka, F. Che, M. Liu, A. Seifitokaldani, Y. Pang, S.-C. Lo, A. Ip, Z. Ulissi and E. H. Sargent, Accelerated discovery of CO₂ electrocatalysts using active machine learning, *Nature*, 2020, **581**(7807), 178–183.
- 157 Z. W. Ulissi, M. T. Tang, J. Xiao, X. Liu, D. A. Torelli, M. Karamad, K. Cummins, C. Hahn, N. S. Lewis, T. F. Jaramillo, K. Chan and J. K. Nørskov, Machine-Learning Methods Enable Exhaustive Searches for Active Bimetallic Facets and Reveal Active Site Motifs for CO₂ Reduction, *ACS Catal.*, 2017, **7**(10), 6600–6608.
- 158 H. Xie, X. Xie, G. Hu, V. Prabhakaran, S. Saha, L. Gonzalez-Lopez, A. H. Phakatkar, M. Hong, M. Wu, R. Shahbazian-Yassar, V. Ramani, M. I. Al-Sheikhly, D.-E. Jiang, Y. Shao and L. Hu, Ta–TiO_x nanoparticles as radical scavengers to improve the durability of Fe–N–C oxygen reduction catalysts, *Nat. Energy*, 2022, **7**(3), 281–289.
- 159 X.-L. Zhang, S.-J. Hu, Y.-H. Wang, L. Shi, Y. Yang and M.-R. Gao, Plasma-Assisted Synthesis of Metal Nitrides for an Efficient Platinum-Group-Metal-Free Anion-Exchange-Membrane Fuel Cell, *Nano Lett.*, 2023, **23**(1), 107–115.
- 160 S. Qin, Y. Duan, X.-L. Zhang, L.-R. Zheng, F.-Y. Gao, P.-P. Yang, Z.-Z. Niu, R. Liu, Y. Yang, X.-S. Zheng, J.-F. Zhu and M.-R. Gao, Ternary nickel–tungsten–copper alloy rivals platinum for catalyzing alkaline hydrogen oxidation, *Nat. Commun.*, 2021, **12**(1), 2686.
- 161 W. Ni, T. Wang, P. A. Schouwink, Y. C. Chuang, H. M. Chen and X. Hu, Efficient Hydrogen Oxidation Catalyzed by Strain-Engineered Nickel Nanoparticles, *Angew. Chem., Int. Ed.*, 2020, **59**(27), 10797–10801.
- 162 F. Yang, X. Bao, Y. Zhao, X. Wang, G. Cheng and W. Luo, Enhanced HOR catalytic activity of PGM-free catalysts in alkaline media: the electronic effect induced by different heteroatom doped carbon supports, *J. Mater. Chem. A*, 2019, **7**(18), 10936–10941.
- 163 P. A. Simonov, O. V. Cherstiouk, A. N. Kuznetsov, V. I. Zaikovskii, T. Y. Kardash, A. G. Oshchepkov, A. Bonnefont and E. R. Savinova, Highly active carbon-supported Ni catalyst prepared by nitrate decomposition with a sacrificial agent for the hydrogen oxidation reaction in alkaline medium, *J. Electroanal. Chem.*, 2019, **852**, 113551.
- 164 G. Wang, W. Li, B. Huang, L. Xiao, J. Lu and L. Zhuang, Exploring the Composition–Activity Relation of Ni–Cu Binary Alloy Electrocatalysts for Hydrogen Oxidation Reaction in Alkaline Media, *ACS Appl. Energy Mater.*, 2019, **2**(5), 3160–3165.
- 165 Y. Gao, H. Peng, Y. Wang, G. Wang, L. Xiao, J. Lu and L. Zhuang, Improving the Antioxidation Capability of the Ni Catalyst by Carbon Shell Coating for Alkaline Hydrogen Oxidation Reaction, *ACS Appl. Mater. Interfaces*, 2020, **12**(28), 31575–31581.



